Low Carrier Effective Masses in Photoactive Sr2Sb2O2Q3 (Q = S, Se): The Role of the Lone Pair

Sandy Al Bacha, Sébastien Saitzek, Pascal Roussel, Marielle Huvé, Emma Mccabe, Houria Kabbour

Low carrier effective masses in photoactive $Sr_2Sb_2O_2Q_3$ (Q = S, Se): the role of the lone pair

Sandy Al Bacha[a,b,c], Sébastien Saitzek[d], Pascal Roussel[a], Marielle Huvé[a], Emma E. McCabe[c]*, Houria Kabbour[a]*

[a] Univ. Lille, CNRS, Centrale Lille, ENSCL, Univ. Artois, UMR 8181 – UCCS – Unité de Catalyse et Chimie du Solide, F-59000 Lille, France.

[b] University of Kent, School of Physical Sciences, Canterbury, Kent CT2 7NH, U.K.

[c] Durham University, Departement of Physics, Durham DH1 3LE, U.K.

[d] Univ. Artois, CNRS, Centrale Lille, Univ. Lille, UMR 8181, Unité de Catalyse et Chimie du Solide (UCCS), F-62300 Lens, France.

Corresponding authors: emma.mccabe@durham.ac.uk , houria.kabbour@univ-lille.fr

ABSTRACT

The crystal structure, electronic properties, photocatalytic activity and photocurrent response of a new antimony oxysulfide $Sr_2Sb_2O_2S_3$ and its oxyselenide analogue $Sr_2Sb_2O_2Se_3$ are presented. Both oxychalcogenides contain heteroleptic $SbOQ_4$ units with stereochemically-active $5s^2$ electron pairs. Our combined experimental and computational study highlights the structure-property relationships in this family of materials. By means of density functional theory calculations, we show a very low effective mass for the electrons (m_e^* = 0.191(6), 0.163(2) m_0) and holes (m_h^* = 0.276(2), 0.190(2) m_0) for the oxysulfide and the oxyselenide, respectively, indication of very high mobilities. Using DFT calculations, we attributed the low effective masses values (related to the curvature of the bands) to the nature and strength of the bonding between the lone pair electrons and the anions in the studied structure compared with other structure ($Sr_6Cd_2Sb_6S_{10}O_7$). We analyze the states contributing to the lone pair stereoactivity and consequently to the observed photocurrent response and photocatalytic behaviour under solar irradiation. This activity, and the bandgap values and band-edge positions illustrate the potential of these antimony oxychalcogenides as promising candidates for water splitting using solar energy. Our study, unlock some key features in designing oxysulfides with low effective masses, advantageous for photocatalysis.

INTRODUCTION

The sustainable production of hydrogen, for energy production using fuel cells, is a current goal in our challenge to meet society's energy demands.[1] Photocatalytic water splitting is one route to produce hydrogen, and is sustainable if this can be achieved using visible light (rather than higher energy UV radiation). However, the use of visible light places constraints on the photocatalytic semiconductor: it must have a bandgap in the range 1.23 - 3.1 eV, and its conduction band minimum (CBM) and valence band maximum (VBM) compatible with the redox potential of water (i.e. the CBM more negative than the reduction potential of H_2O/H_2 (0 V) and the VBM more positive than the oxidation potential of O_2/H_2O (1.23 V)).[2] Whilst many oxide photocatalysts have shown good performance (such as $K_2La_2Ti_3O_{10}$ (2186 and 1131 μmol.h^{-1} for H_2 and O_2 evolution, respectively)[3] and Bi_2MO_6 (k_{app} = 6.3×10^{-3} and 1.7×10^{-3} min^{-1} for W and Mo, respectively,for rhodamine B degradation)[4]), they typically have large band gaps (e.g. 3.5 eV for $K_2La_2Ti_3O_{10}$) and are only photocatalytically active under UV irradiation.[5,6,7,8] This has motivated research to turn towards mixed-anion materials in the search for stable and efficient visible light photocatalysts.[9,10] On another hand, the Aurivillius phases Bi_2MO_6 (M = Mo, W) have smaller band gaps (2.6 eV and 2.8 eV for Bi_2MoO_6 and Bi_2WO_6, respectively) due in part to the contribution from Bi^{3+} $6s^2$ states to the top of the valence band[4], suggesting that "inert pair" ns^2 cations (such as Sb^{3+}) might be advantageous in tuning the band gap in potential photocatalysts.

Oxychalcogenides have attracted attention due to their wide range of properties including magnetism,[11,12] photocatalysis, and electrochemistry.[13,14] In the context of visible-light water splitting, oxysulfides were seen as potential photocatalysts because the sulfide's electronegativity can lead to an increase in the valence band potential and therefore a decrease in the bandgap to the visible range.[15] Within the oxychalcogenide family, many materials adopt layered structures which allow ordering of the anions into more ionic (O^{2-}) and more covalent (Q^{2-} = S^{2-}, Se^{2-}, Te^{2-}) layers.[16] The layered crystal structure tends to give a highly anisotropic electronic band structure, interesting electronic properties and high mobilities of charge carriers.[17] Finally, depending on judicious choice of ions, oxychalcogenides with heteroleptic (O^{2-} and Q^{2-}) coordination of key cations can also be prepared. These heteroleptic coordination environments are often polar, which can enhance electron – hole separation, giving better photocatalytic performance.[18,19,20] According to literature, several oxysulfides were found to be stable with good performances for water splitting with a

suitable bandgap energy in the visible range. $Y_2Ti_2O_5S_2$ demonstrated its stability with an efficient stoichiometric production for both H_2 and O_2,[21] and $LaOInS_2$ polymorphs for a moderate H_2 production.[22,23]

Another important feature for photocatalysis is the charge carriers' dynamics, their effective masses thus their mobility; which can have an impact on the semiconductor performance.[24,25] Oxide materials with a difference in their charge carriers effective masses exhibit a difference in character between the valence and conduction band,[26] as the VB tends to be flat because of the localized oxygen *p* character, giving large hole effective masses, whilst the CB is more dispersive because of the contribution of cations, giving low electron effective masses.[27,28] For example, in a typical post-transition metal-based oxide semiconductor with low electrons and holes effective masses, both CBM and VBM are dispersed because of the unoccupied 5*s* orbitals of the post-transition metal and the orbitals of the neighboring cations overlapping, and of the interaction of the occupied post transition metal 5*s*/3*d* orbitals with anion *p* orbitals, respectively.[29,30,31,32] On the other hand, a recent study on tin oxyselenide demonstrated that introducing a chalcogenide Q^{2-} with its higher energy level and larger ionic radius can reduce the bulk/interface trap states, leading to an enhanced carrier mobility.[33] A small number of oxysulfides and oxyselenides have gained attention for their low holes effective masses such as tetragonal-ZrOS (0.24 m_0) and cubic-ZrOS (0.37 m_0),[34] $SnSe_xO_{1-x}$ (m_h*= 0.58, 0.93, 1.99 for x = 0.22, 0.56 and 0.74 respectively).[33]

We report here $Sr_2Sb_2O_2S_3$ oxysulfide, analogue to the recently discovered oxyselenide $Sr_2Sb_2O_2Se_3$ that adopts a structure comprising double chains of edge-linked $SbSe_4O$ square-based pyramids (Figure 1a).[35] Alongside the synthesis and structural characterization of these antimony oxychalcogenides, diffuse reflectance measurements suggest direct band gaps of 2.44(1) and 1.72(1) eV for $Sr_2Sb_2O_2S_3$ and $Sr_2Sb_2O_2Se_3$, respectively, well matched to the solar spectrum. Photocurrent measurements revealed that both materials exhibit an activity under sunlight with and without external potential, as well as the capacity to degradate the rhodamine B. Electronic structure calculations indicate that the top of the valence band is primarily composed of Sb^{3+} and S^{2-}/Se^{2-} states, as well as revealed a very low electrons and holes effective masses, indication of high mobilities for both compositions.

METHODS SECTION

Single-phase samples of $Sr_2Sb_2O_2Q_3$ (Q = S, Se) (1 g) were synthesized by solid-state reaction from stoichiometric mixtures of the precursors: SrS/Sb_2O_3/Sb/S (Alfa Aesar 99.5%) in the molar ratio 2:0.667:0.667:1 for the oxysulfide and SrO/Sb/Se (Alfa Aesar 99.5%) in the molar ratio 2:2:3 for the oxyselenide. Mixing and grinding were carried out in an argon-filled glovebox due to the air sensitivity of some reactants. Mixtures were then pelletized and heated in an evacuated sealed carbon coated quartz tube. Thermal treatment consisted on heating up to 700 °C and 800 °C for $Sr_2Sb_2O_2S_3$ and $Sr_2Sb_2O_2Se_3$, respectively at a rate of 70 °C/h and dwelling for 48 h before cooling down to room temperature. Upon grinding the pellets, orange and grey powders were obtained for the oxysulfide and the oxyselenide, respectively.

Powder x-ray diffraction (XRPD) data were collected on a Bruker D8 A25 diffractometer equipped with a Lynxeye XET linear detector (Cu Kα) in Bragg−Brentano geometry at room temperature with a 1 s counting time and 0.02 ° step angle. Rietveld refinements were carried out using Topas Academic software.[36,37] The background, sample height, lattice parameters, peak profiles, atomic positions and a global atomic displacement parameter (per phase) were refined. XRPD data were collected in reflection mode and preferred orientation was observed in some sets of data, as a result of the sample packing method. This was modelled in Rietveld refinements using a March-Dollase function along one direction.[38] Despite this additional correction in the refinements, they demonstrate the high quality of the samples prepared.

Transmission electron microscopy diffraction study was performed on a FEI Technai G2-20 twin microscope. The powder was crushed and dropped in the form of an alcohol suspension on carbon-supported copper grids, followed by evaporation under ambient conditions.

Diffuse-reflectance of the sample was measured from 200 to 900 nm using a PerkinElmer Lambda 650 spectrophotometer**.**

Scanning electron microscopy (SEM) experiments and energy dispersive X-ray (EDX) analysis were carried out on a Hitachi S3400N microscope.

The thermal stability of $Sr_2Sb_2O_2S_3$ was investigated by thermogravimetric analysis (TGA) using a TGA-92 thermobalance under pure argon; coupled with thermal dilatometric analysis (TDA) at first then with mass spectrometry (MS). The evolved gases were monitored by an Omnistar quadrupole mass spectrometer (Pfeiffer). The atmosphere was controlled by evacuating

and then filling the thermobalance with the carrier gas before the sample was heated to 1000 °C at a rate of 5 °C/min.

Density functional theory (DFT) calculations were carried out using the projector-augmented-wave method[39,40] encoded in the Vienna *ab initio* simulation package (VASP)[41] and the generalized gradient approximation (GGA) of Perdew, Burke and Ernzerhof[42] for the exchange-correlation functionals. Full geometry optimizations were carried out using a plane-wave energy cutoff of 550 eV and a threshold of the self-consistent-field energy convergence of 10^{-6} eV were used with ƙ-points meshes (4×13×3) in the irreducible Brillouin zone for $Sr_2Sb_2O_2Q_3$ (Q = S, Se). The relaxed structure was a good match (reasonable deviation not exceeding few percentages for the unit cell parameters) with the experimental structure (see unit cell parameters and atomic positions of the relaxed structures in the SI), and it was used for calculations of the electronic band structure, the charge carrier's effective masses and the density of states. Vesta software[43] was used to visualize the crystal structure and the localized electron densities. The COHP (Crystal Orbital Hamilton Population) analysis was carried out in the framework of the LOBSTER software.[44,45,46]

The photo-reactor consisted of a 200 ml flask irradiated from above and aluminum foil covers to prevent radiations exposure. First, the solution (containing 200 mL of Rhodamine B (5×10^{-6} mol dm^{-3}) and 100 mg of the photocatalyst powder ($Sr_2Sb_2O_2Q_3$ (Q = S, Se)) were placed in an ultrasound for 20 mins (to break up agglomerates) and stirred for 30 mins in the dark to ensure an appropriate adsorption/desorption equilibrium. This test was performed under UV (254 nm, 40 W) and solar (100 mW cm^{-2}) irradiations. Then, samples were taken, at regular intervals to monitor the evolution of the concentration of the photodegraded Rhodamine B by spectrophotometry. Absorbance measurements were carried out using a Shimadzu UV-2600 UV-visible spectrophotometer.

The electrochemical device (Autolab PGSTAT204, Metrohm) coupled to a LED module (LED driver kit, Metrohm) was used to collect the photocurrent measurements. The LEDs (450, 470, 505, 530, 590 and 627 nm with low spectral dispersion) were calibrated using a photodiode to determine the density of the luminous flux received by the sample. The photoelectrochemical measurements were performed in standard three-electrode cell (Magnetic Mount Photo-electrochemical Cell (Redox.me®), including Ag/AgCl and Pt wire acted as reference electrode and counter electrode, respectively. This cell allows standardized illumination over 1 cm^2 by the backside of the working

electrode. The working electrode consisted of the photocatalyst powder dispersed in PVDF (polyvinylidene fluoride) binder (in 2:1 ratio), that was later deposited on an ITO/glass substrate (Delta Technologies, Ltd), using the drop casting technique.[47] The electrolyte employed is an aqueous 0.1 M sodium sulfate (Na_2SO_4) solution.

RESULTS

Polycrystalline Phase Analysis. Small single crystals of $Sr_2Sb_2O_2S_3$ were first identified by serendipity in some attempts to prepare another compound, namely $Sr_6Zn_2Sb_6O_7S_{10}$. After optimising the synthesis method for $Sr_2Sb_2O_2S_3$, a high-purity sample (without Zn) was prepared. The method was optimized by using stoichiometric amounts of reagents based on preliminary investigations using single crystal X-ray diffraction and EDX, and then finding the optimal synthesis temperature of 700°C as noted above. Preliminary analysis of XRPD data (see supporting information) indicated a model consistent with the previously reported Se analogue, $Sr_2Sb_2O_2Se_3$,[35] in the $P2_1/c$ space group with, as excepted, a slightly smaller unit cell volume (room temperature volume = 404.68 (2) $Å^3$ - see SI, compared with 432.81 $Å^3$ for $Sr_2Sb_2O_2Se_3$). EDX analysis of the Sr, Sb and S content revealed a Sr:Sb:S ratio of 28.3:29.0:42.7, in good agreement with the expected stoichiometry of $Sr_2Sb_2O_2S_3$ (Figure 1b). A sample of $Sr_2Sb_2O_2Se_3$ was also prepared following the method reported by Panella et al.[35]

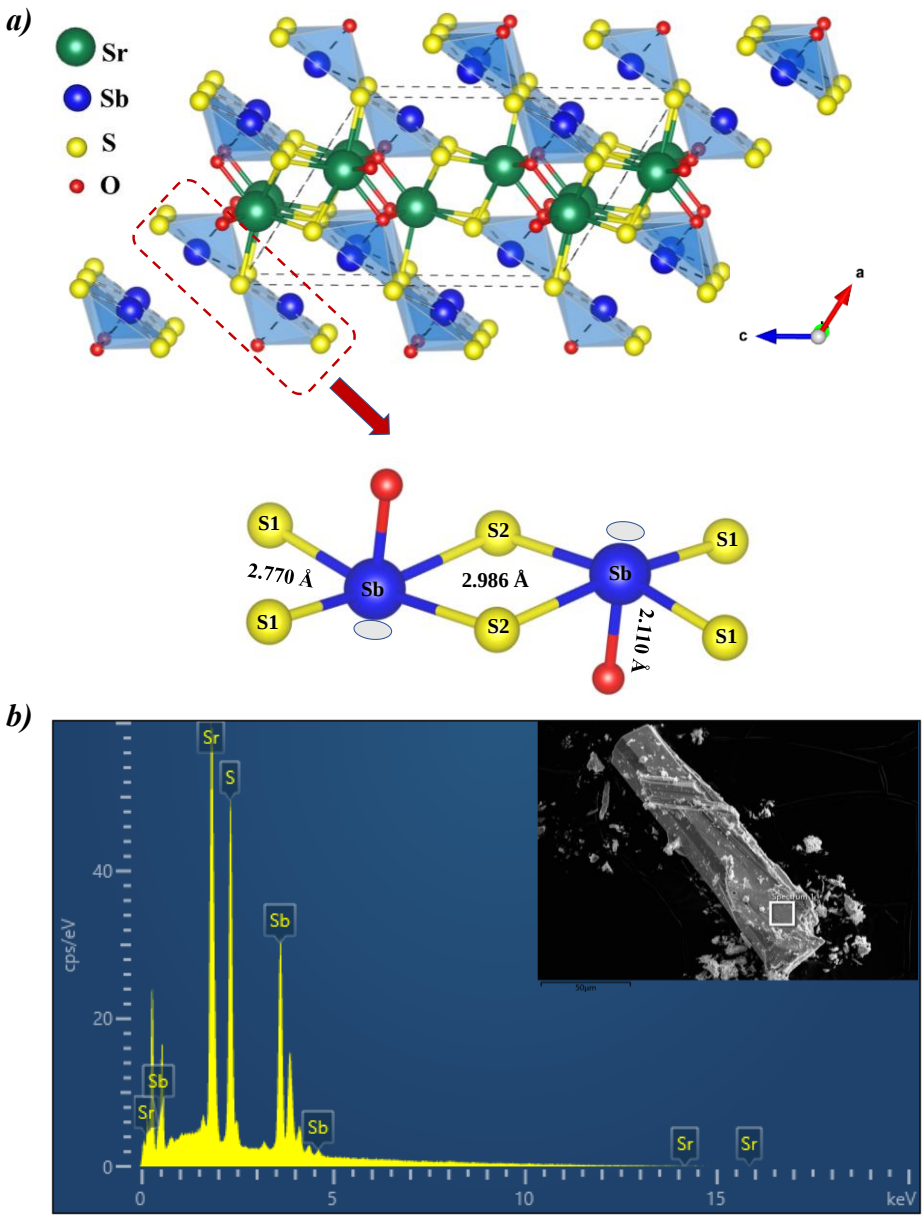

Figure 1 : (a) View of the $P2_1/c$ model of $Sr_2Sb_2O_2S_3$ with the coordination environments and distances of Sb ions. (b) Spectrum of the EDX analysis of a $Sr_2Sb_2O_2S_3$ crystal.

Other distortions to give various *C*-centred monoclinic structural models were also considered but gave no significant improvement in fit. Alternately, a preliminary crystallographic study using single crystal X-ray diffraction and electron diffraction data was conducted which revealed a more complex structure: electron diffraction data reveal additional reflections that can only be indexed

by incommensurately-modulated structures which may vary between domains (see supporting information) and a more detailed structural study is underway.

Thermal Stability. The thermal stability of $Sr_2Sb_2O_2S_3$ was studied using TGA coupled with TDA (Figure 2a) then coupled with mass spectrometry under argon in both cases going up to 1000 °C (Figure 2b). No weight loss was associated with the endothermic peak at ~ 735 °C on the TDA curve (lower panes), suggesting a phase transition at this temperature. Above 800 °C, two weight losses were detected coupled with three exothermic combined peaks that indicated a phase degradation. A structural phase transition could not be confirmed by high temperature XRD due to insufficient information about the fusion temperature.

To investigate possible phase degradation, TGA was coupled with MS with the same conditions (under argon, in the range 25-1000 °C). No loss of water was observed (no signal at *m/z* 18). Signals were measured (lower panes) at *m/z* 64 (SO_2^+), *m/z* 48 (SO^+) and *m/z* 44 (CO_2) allowing the evolved gases to be identified. A sharp mass loss (8.1 %) occurs at around 800 °C, close to the theoretical mass loss expected for the loss of 1 molecule of sulfur monoxide (SO) (8.8 %). This was confirmed by EDX (see supporting information) on the residue after TGA-MS measurements where the atomic percentages corresponding to the sulfur element decreased.

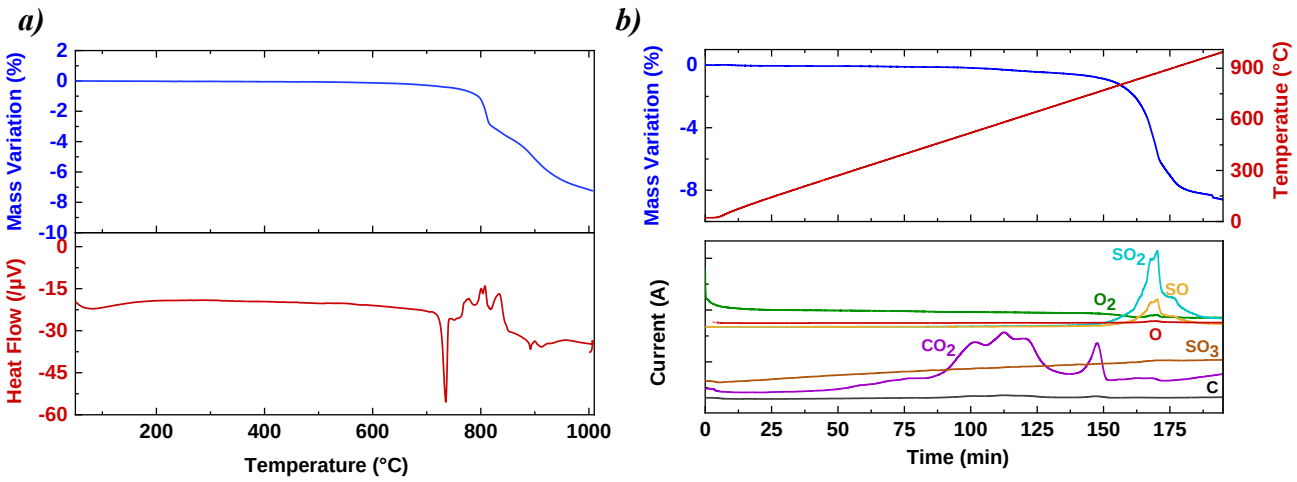

Figure 2 : (a) TGA (upper panes) coupled with TDA (lower panes) of $Sr_2Sb_2O_2S_3$ under argon (b). TGA (upper pane) coupled with mass spectrometry (lower panes) of $Sr_2Sb_2O_2S_3$ under argon. The mass variation and temperature are given as a function of time.

Optical Measurements. Optical properties of the polycrystalline $Sr_2Sb_2O_2S_3$ and $Sr_2Sb_2O_2Se_3$ phases were investigated by measuring the reflectance using UV-Visible spectroscopy. Reflectance *vs.* wavelength analysis is shown in Figure 3. The Kubelka-Munk transformation $F(R)=(1-R)^{(1/n)}/2R$[48] was applied to the reflectance and the optical band gap, E_g, was determined using the Tauc plot method[49] by drawing $[F(R)h\upsilon]^{1/n}$ vs. $[h\upsilon]$ (where $h\upsilon$ is the photon energy). Assuming a direct allowed transition (n= 1/2) (see the results from DFT calculation, presented below), E_g was determined to be 2.44(1) eV and 1.72(1) eV for $Sr_2Sb_2O_2S_3$ and $Sr_2Sb_2O_2Se_3$, respectively; convenient for the solar spectrum, and comparable with other reported mixed-anion materials including oxynitrides $LaTiO_2N$ (2.1 eV),[50] $XNbO_2N$ (X= Ca, Sr, Ba, La)[51] and lone-pair containing oxyfluorides Bi_2NbO_5F (2.86 eV), Bi_2TaO_5F (2.95 eV).[52]

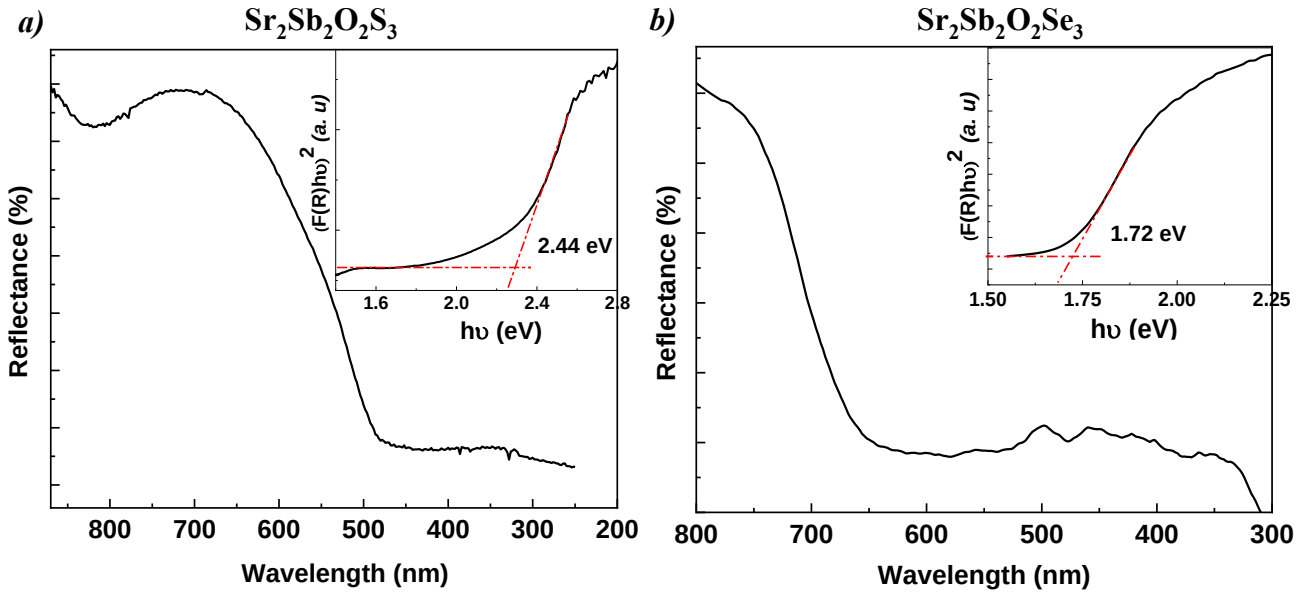

Figure 3 : Diffuse-reflectance spectra with a Tauc plot inset to determine the experimental band gap of a) $Sr_2Sb_2O_2S_3$ and b) $Sr_2Sb_2O_2Se_3$.

First principles Calculations. DFT calculations were carried out to investigate the electronic band structures of $Sr_2Sb_2O_2Q_3$: calculations were carried out using both the reported $P2_1/c$ models and the higher symmetry $C2/m$ models (described above). This choice of symmetry has minimal effect on the results from these electronic structure calculations (because the additional parameters allowed by the $C2/m$ model are in fact very close to the ideal values of the $P2_1/c$ model). Results for the $P2_1/c$ models are presented here whilst those for the $C2/m$ models are given in the supporting

information for comparison. DFT calculations revealed direct band gaps of 1.09 eV and 0.73 eV for *Q* = S, Se, respectively. These are smaller than the experimental optical band gaps (2.44(1) eV and 1.72 eV measured for $Sr_2Sb_2O_2S_3$ and $Sr_2Sb_2O_2Se_3$, respectively) discussed above. This might be explained by the GGA approximation (with PBE functional used here) well known to underestimate band gaps.[42] Figures 4a and 4d show the calculated electronic band structure for $Sr_2Sb_2O_2Q_3$ with valence band maximum and conduction band minimum at the Γ point (0; 0; 0) for both *Q* = S, Se.

The projected densities of states are shown in Figures 4b and 4e focusing on the region around the Fermi level of the valence and conduction band. The orbitals near this selected region are mainly dominated by Sb and S/Se states, while Sr and O states make a minimal contribution. The Sb 5*p* states dominate the conduction band minimum, lying from ~1 eV up to ~3 eV, while the Sb 5*s* states lie in the valence band (in the range of -1.5 to -0.1 eV), hybridizing with the O 2*p* and S 3*p*/Se 4*p* to form the maximum of the valence band. This orbital contribution to both bands was also confirmed by the plot of the fat bands (see supporting information), and similar results have been reported for $Sm_2Ti_2S_2O_5$,[53] and $Ln_2Ti_2S_2O_5$.[54]

Similar Sb 5*s* contribution to the top of the valence band was also observed for several antimony based compounds including $Sr_6Cd_2Sb_6S_{10}O_7$ oxysulfide,[55,20] α-Sb_2O_3, β-Sb_2O_3, γ-Sb_2O_3, α-Sb_2O_4 and β-Sb_2O_4 oxides[56] and Sb_2S_3 and Sb_2Se_3 chalcogenide semiconductors.[57] This Sb 5*s* - *Q* n*p* (*Q* = O, S, Se) hybridisation plays a key role in reducing the band gap into the visible range.

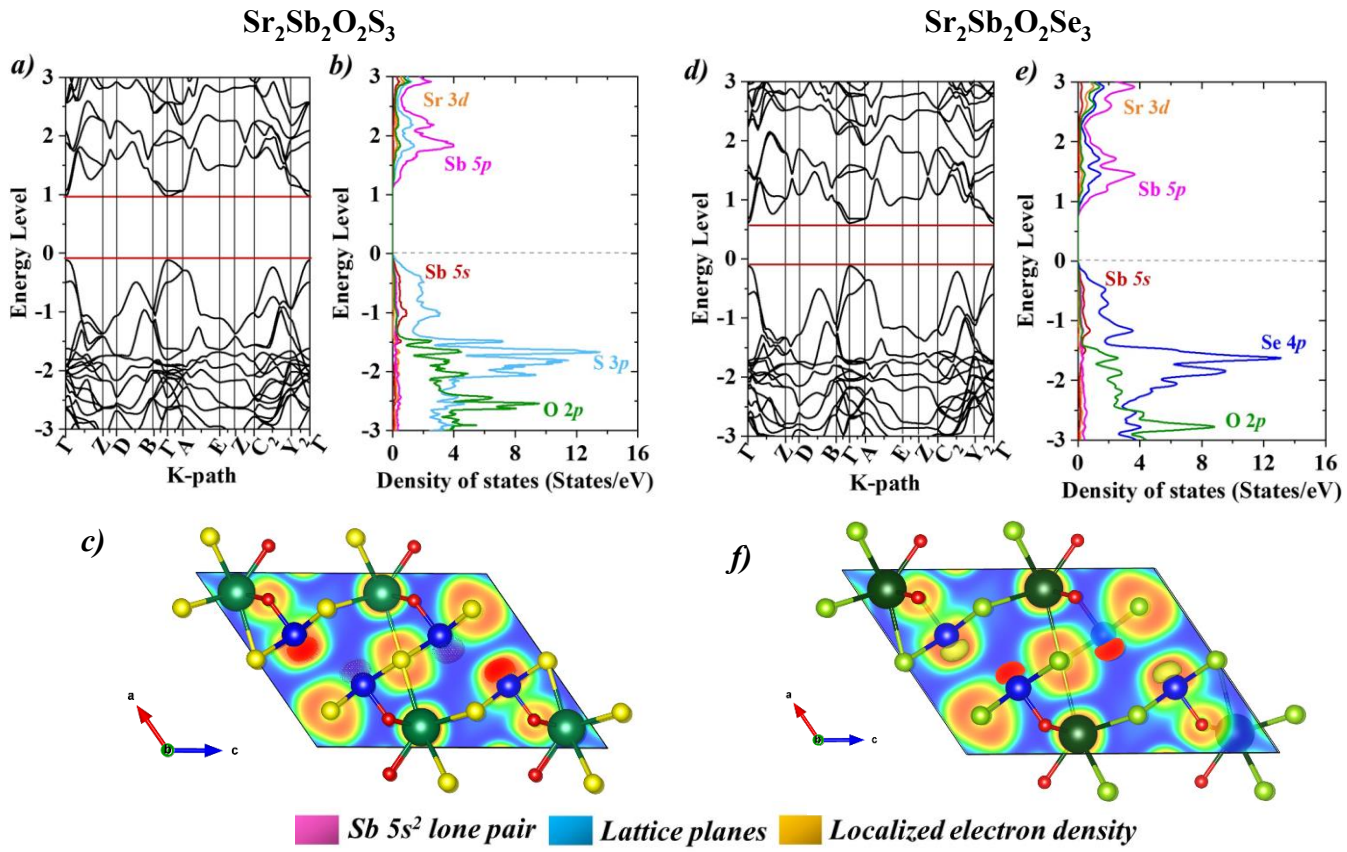

Figure 4 : (a) and (d) Electronic band structure, (b) and (e) Projected DOS is shown for the Sr 3*d*, Sb 5*s*, Sb 5*p*, S 3*p*/ Se 4*p* and O 2*p* states. The Fermi level is set to 0, (c) and (f) Local electron density projected on the (010) lattice plane and 0.91 isosurface levels of DFT plots of $Sr_2Sb_2O_2S_3$ and $Sr_2Sb_2O_2Se_3$, respectively, for the $P2_1/c$ model.

In order to have a quantitative investigation of the charge carriers' mobilities, the effective masses of electrons (m^*_e) and of holes (m^*_h) were calculated[58] using the following equation near the CBM and the VBM at Γ (0; 0; 0):

$$\left(\frac{1}{m^*}\right)_{ij} = \frac{1}{\hbar^2}\frac{\partial^2 E_n(k)}{\partial k_i k_j} \qquad (1)$$

where $E_n(k)$ corresponds to the n^{-th} electronic band in *k*-space. Prior to the effective masses' extraction, the self-consistent electronic calculation was followed by a non-self-consistent calculation along the high symmetry lines. Different dispersions were observed at the CBM and VBM, which suggests different mobility of electrons and holes. We investigated the directions

within the layers, $\Gamma \rightarrow A$, $\Gamma \rightarrow B$, $\Gamma \rightarrow Z$ and $\Gamma \rightarrow Y_2$, very near to the Γ point, since the VBM and the CBM are located at Γ for both phases.

The calculations revealed low effective masses for both oxyselenide and oxysulfide phases (Table 1), with particularly low values for electron (0.163(2) m_0 for $\Gamma \rightarrow Z$) and hole (0.190(2) m_0 for $\Gamma \rightarrow A$) effective masses for the oxyselenide. The carrier mobility is inversely proportional to the effective mass; therefore, this high mobility makes the oxyselenide particularly attractive for efficient photoconduction and photocatalysis applications. These values are lower than those reported for related oxyselenide and oxysulfide materials (m_e* values of 0.59 m_0, 0.68 m_0 for BiCuOS and BiAgOS, respectivel;[59] m_h* of 0.24 m_0 and 0.37 m_0 for c-ZrOS and t-ZrOS, respectively;[34] m_e*= 1.6(2) m_0 for LaCuOSe;[60] m_h*= 0.58, 0.93, 1.99 m_0 for $SnSe_xO_{1-x}$).[33] The high mobilities reflect the high dispersion at the VBM and CBM, influenced by both the high covalency (particularly for the oxyselenide), and the presence of the stereochemically-active $5s^2$ electron pair on Sb^{3+} ions (as discussed further below).

Table 1. Calculated electron (m_e^*) and hole (m_h^*) effective mass, m_0 being the free electron mass for $Sr_2Sb_2O_2Q_3$ for $P2_1/c$ model.

Directions	$Sr_2Sb_2O_2S_3$		$Sr_2Sb_2O_2Se_3$	
	m_e/m_0	m_h/m_0	m_e/m_0	m_h/m_0
$\Gamma \rightarrow A$	1.958(8)	0.718(4)	1.393(1)	0.447(7)
$\Gamma \rightarrow B$	0.651(8)	0.276(2)	0.428(3)	0.190(2)
$\Gamma \rightarrow Z$	0.191(6)	0.848(7)	0.163(2)	0.525(2)
$\Gamma \rightarrow Y_2$	1.681(2)	1.482(2)	1.656(2)	1.013(1)

The Sb 5*s* - *Q* n*p* hybridisation relates to the Sb $5s^2$ lone pair and its stereochemical activity. The valence electron density map projected on the (010) plane is shown in Figure 4c and 4f giving insight into the stereoactivity of the Sb^{3+} lone pair within the $O(S,Se)_4$ heteroleptic environment. More generally, the stereochemical activity of lone pairs are known to bring crystalline anisotropy and their benefits on several properties have been put forward in different type of materials. Recently, theoretical studies have been reported for reduced main group cations (in oxides) such as the lone pair cation Sn^{2+} (discussed later, ref. 84) where high charge carriers' mobility is mostly related to the lone pair states and the overlap between the s orbital of the lone pair cation and the anions states. Another example in chalcogenides are the well-known Sb_2S_3 and Sb_2Se_3 semiconductors which were also theoretically studied for lone pair related anisotropic effects (effective masses and mobility) to provide guidelines for using their features to design efficient

solar cells devices [57]. Similar effects were also observed for Sb-based compounds[61] such as $Sr_6Cd_2Sb_6S_7O_{10}$,[20] $Sr_6Cd_2Sb_6Se_7O_{10}$[19] and Bi-based with a $6s^2$ stereoactive lone pair.[62]

To quantify this stereochemical activity, a universal method described by Hu *et al.*[63,64] was adopted, in order to calculate the ratio of the stereochemical activity R_{SCA} which involves integrating the PDOS of Sb states from a specified energy level (the point where the intensity of Sb-*s* and Sb-*p* is equivalent) to the Fermi level (set at 0). This makes the R_{SCA} sensitive to the choice of energy range depending on the orbitals of the chosen lone pair cation. R_{SCA} was calculated to be 0.68 and 0.54 for the antimony lone pair within the SbS_4O and $SbSe_4O$ entities, respectively (Table 2 and supporting information). In our previous study on $Sr_6Cd_2Sb_6S_{10}O_7$,[20] we found a R_{SCA} of 0.57, 0.59, 0.64 for SbS_5, SbS_4O and SbO_3, respectively. This is an indication that the presence of an heteroleptic environment (coordinated with both sulfide/selenide and oxide anions) around the antimony influence its stereochemical activity; in a way that with increasing the anion ionicity, this activity increases (see ref. 20 and references therein in which the correlation with the DFT calculated lone pair volume is also consistent with this evolution).

Table 2. Integrated PDOS from a specified energy level to the Fermi level and the calculated stereochemical activity factor for the SbS_4O and $SbSe_4O$ entity.

	SbS_4O entity	**$SbSe_4O$ entity**
I (Sb-s)	1.6	1.3
I (Sb-p)	2.33	2.39
R_{SCA}	0.68	0.54

The Crystal Orbital Hamiltonian Population (COHP) calculation give access to projected contributions on specific bonds with the dispersion but also an integral value representing the nature (bonding/antibonding) and strength of the bond in average. The ICOHP obtained for some representative border distances seem to have an evolution mostly depending on the distance with similar average distances in both compounds. On another hand, the dispersion of the p-COHP allows a better comparative study (Figure 5). In the case of the $Sr_2Sb_2S_3O_2$ phase, the Sb-S antibonding states (that relate to the Sb $5s^2$ lone pair, as defined by the revised model[65,66]) extend from the Fermi level much deeper into the valence band, compared with $Sr_6Cd_2Sb_6S_{10}O_7$.[20] It is

equivalent to greater curvature of bands used to determine the m_h^* and constitute one explanation for the lower m_h^* in $Sr_2Sb_2S_3O_2$.

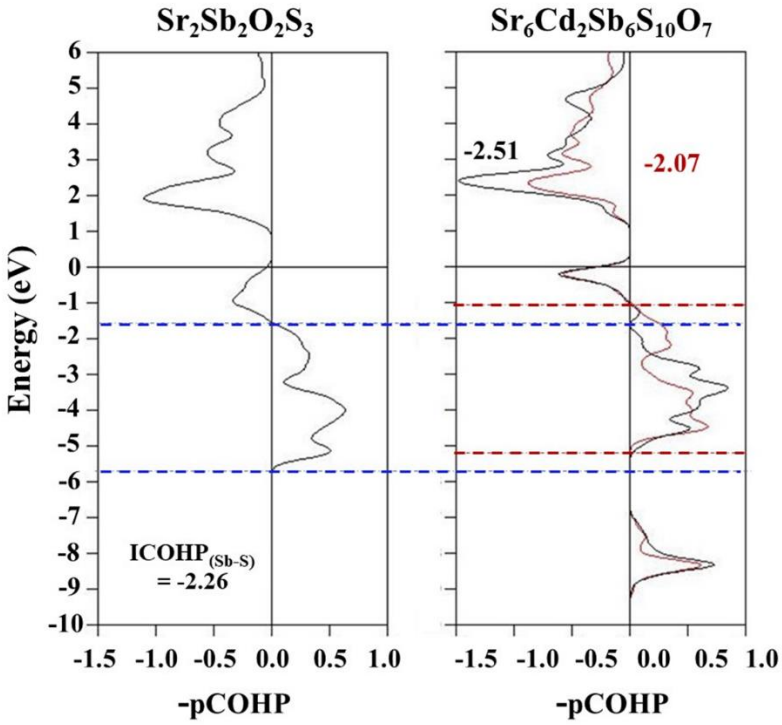

Figure 5 : (left) Projected COHP (p-COHP) for $Sr_2Sb_2O_2S_3$ phase on one of the 1D unit "border" Sb-S bond calculated with the *C*2/*m* optimized structure, and (right) p-COHP for the phase $Sr_6Cd_2Sb_6S_{10}O_7$ on the Sb-S bond located at two opposite borders of the 1D (in red and black) unit. Dashed blue and red lines represent the extend of the Sb-S antibonding states in the valence band and of the lower bonding states.

Electrochemical measurements. The chronoamperometric measurements (showing the variation in current density Δj as the difference between the illuminated (j_{ill}) and the dark current densities (j_{dark})) were carried out for $Sr_2Sb_2O_2Q_3$ (*Q* = S, Se). Measurements were carried out for thick films of $Sr_2Sb_2O_2S_3$ under 450 nm with several irradiances for illumination and dark cycles (Figure 6). Without external bias voltage, the transient photocurrent increased from 1.7×10^{-1} µA cm^{-2} for a 22 mW.cm^{-2} power density to 2.2×10^{-1} µA cm^{-2} for 42 mW.cm^{-2} and kept increasing more slowly until reaching a stable photocurrent of 2.65×10^{-1} µA cm^{-2} for 111 mW.cm^{-2} (Figure 6a). Figure 6b presents the evolution of the photocurrent Δj with the intensity of the luminous flux Φ_0 according to a classical power law[67] giving a curve going through the origin with an equation of $\Delta j = 8.10\times10^{-2}\Phi^{0.25}$. For an ideal trap-free system, the exponent is equal to 1. In our

case, the fitting gives a non-unity (i.e. 0.25(2)) exponent, suggesting a complex process of electron-hole generation, recombination and trapping within the sample. Moreover, for high light intensities, the photocurrent becomes independent of the light intensity received. This effect can be due to a saturation of photo-generated electron-hole pairs and/or a limitation of mobility in the layer.[68] The same measurements were performed under 0.4 V bias voltage where the value of the current density increases with the voltage (see supporting information). However, the trend remains the same with a power law whose exponent is low (0.18(2)) indicating that for high powers most of the traps are already filled in and further illumination power cannot effectively increase the photogain.[69]

The produced photocurrent is naturally linked to the material's absorption, therefore for an orange powder, the best efficiency should be observed in the complementary color spectral area between 450 and 505 nm. This was confirmed by recording the variation of the transient photocurrent Δj for V_{bias}= 0 V *vs.* wavelength (Figure 6c). The highest photocurrent is observed at 505 nm and it decreased towards the longest wavelengths (590 - 627 nm). This result was also observed when a 0.4 V bias voltage was applied (see supporting information).

The photoelectrode was then submitted to solar irradiation (150 W Xenon lamp with AM 1.5G filter – 100 mW.cm^{-2}) and the transient photocurrent response was recorded under different on/off cycles for two bias voltages, 0 and 0.4 V. Figure 6d, shows the response recorded for 0 V bias voltage: a photocurrent of 3.2×10^{-1} µA cm^{-2} is obtained with a slight decrease in the value upon increasing the power density, until stability at the end with a 2.7×10^{-1} µA cm^{-2} value. The response for a 0.4 V potential was also measured (supporting information) and gave a higher photocurrent (1.60 µA cm^{-2}) but with a clear decrease (1.15 µA cm^{-2}) at higher power densities. This behavior indicates the presence of progressive corrosion within the thick film in the chosen electrolyte which may be accentuated by the applied potential. This was also observed after photocatalysis measurements and XRPD analysis of the samples after photocurrent measurements (see below) would be useful to investigate this further. Although photocorrosion may be occurring upon applying a potential in this material, its capacity to generate a photocurrent under sunlight without potential is rarely observed for this family of materials. For instance, [$(Ba_{19}Cl_4)(Ga_6Si_{12}O_{42}S_8)$] generates a transient photocurrent response when subjected to ultraviolet light excitation[70] and $LaGaS_2O$ electrode produces an anodic photocurrent only under UV light.[71] The difference between the responses recorded under sunlight with both potentials (0.4 and 0 V) is consistent with

the reproducibility test under 450 nm excitation and could be explained by the presence of some kind of photocorrosion when applying a potential, caused by the materials' instability in the used electrolyte. This hypothesis is still to be studied and verified by further tests, including testing other electrolytes.

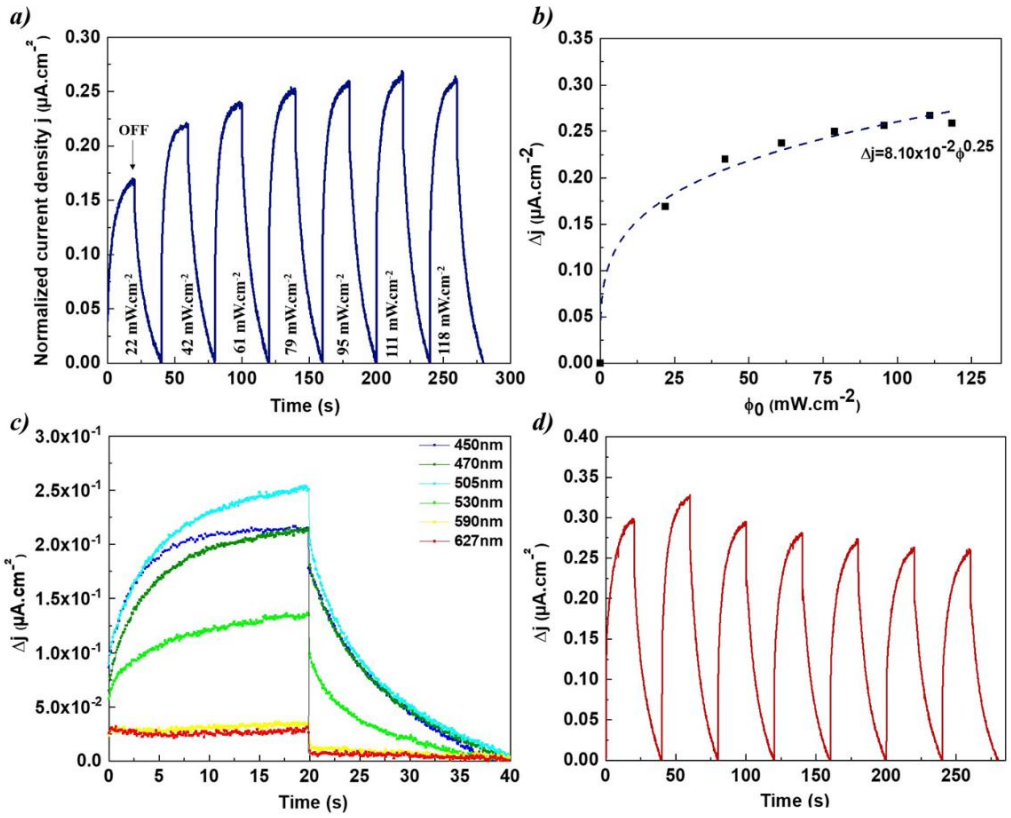

Figure 6 : (a) Transient photocurrent response (V_{bias} = 0 V under a 450 nm excitation) of $Sr_2Sb_2O_2S_3$ (b) Evolution of the photocurrent density the power density of light (c) Transient photocurrent response vs. wavelengths (constant light intensity ϕ_0=42 mW cm^{-2} and Bias = 0 V) of $Sr_2Sb_2O_2S_3$ (d) Transient photocurrent response under solar illumination (100 $mW.cm^{-2}$) for V_{bias}= 0 V.

The photocurrent responses of the previously reported $Sr_2Sb_2O_2Se_3$[35] was also measured with a 0.4 V bias voltage and under excitation of 450 nm (Figure 7). A linear increase in the transient photocurrent was observed under different illumination and dark cycles from 0.8 to 1.1 $\mu A.cm^{-2}$ for a power density of 22 to 111 $mW.cm^{-2}$ (Figure 7a). As for the oxysulfide, the generated photocurrent increased with the intensity of the luminous flux according to a classical power law[67] (Figure 7b) giving a curve going through the origin with an equation of $\Delta j=6.17\times10^{-2}\phi^{0.58}$. In $Sr_2Sb_2O_2Se_3$ the exponent value (0.58) is low, indicating of the presence of many traps (although

fewer than $Sr_2Sb_2O_2S_3$ with exponents of 0.25 and 0.18 for 0 V and 0.4 V, respectively). Unlike the oxysulfide, the photocurrent response registered for $Sr_2Sb_2O_2Se_3$ for 0.4 V (Figure 7a) and 0 V (supporting information) shows the characteristic decay from a "spike", indication of the presence of a competition between two phenomena (transfer and recombination). This can be explained by the rapid separation of the electron/hole pairs under illumination, then the establishment of an equilibrium state between the recombination and the transfer of the carriers. In fact, at 0.4 V, the photocurrent peak is more square and shorter than that observed at 0 V, indicating more ideal behavior at 0.4 V, as the equilibrium is reached faster (giving a more square peak), and minimal recombination occurs (shorter peak). We can also note that without applied potential, the photocurrent generated tends toward a saturation value from 42 $mW.cm^{-2}$ (supporting information). Whilst at V_{bias} = 0.4 V, we observe classical power law behavior (Figure 7b) without reaching saturation. To understand this behavior, it is possible in the case of a 'spike' to calculate the transfer and recombination constants according to a model proposed by Parkinson *et al*.[72] In this model, the time constant of the decay is given by expression (2):

$$\frac{j(t)-j(\infty)}{j(0)-j(\infty)} = e^{-\frac{t}{\tau}} \qquad \text{with} \qquad \tau = \frac{1}{k_{rec}+k_{tr}} \tag{2}$$

where τ, k_{rec} and k_{tr} are the time constant, recombination rate constant and transfer rate constant, respectively.

Moreover, the ratio of the steady state photocurrent to the instantaneous photocurrent observed when the illumination is switched on is given by expression (3)[73]:

$$\frac{j(\infty)}{j(0)} = \frac{k_{tr}}{k_{tr}+k_{rec}} = \eta_{tr} \tag{3}$$

These two expressions make it possible to calculate the values of k_{tr}, k_{rec} and η_{tr} (transfer efficacity). This model was applied to extract the values of k_{tr}, k_{rec} as a function of light intensity for V_{bias} = 0 and 0.4 V (supporting information). At 118 $mW.cm^{-2}$, the rate constants at 0.4 V are k_{tr} = 7 min^{-1} and K_{rec} = 1.5 min^{-1} (i.e. a transfer efficiency of 85 %, supporting information), and k_{tr} = 0.1 min^{-1} and K_{rec} = 1.3 min^{-1} (i.e. a transfer efficiency of 10 %, supporting information) at 0 V.

The photocurrent dependency on the wavelengths recorded for 0.4 V bias voltage is shown in Figure 7c for $Sr_2Sb_2O_2Se_3$, and shows a similar response to that recorded for the oxysulfide analogue (supporting information). The best efficiency was seen for 450 nm excitation with the highest photocurrent value of 1.95 $\mu A.cm^{-2}$ and decreasing proportionally towards longer wavelengths. However, a significant photocurrent is observed over the entire spectral range (450 to 655 nm) unlike the oxysulfide where the photocurrent drops drastically from 590 nm. To finish, the photoelectrode was exposed to solar irradiation (Figure 7d) which showed good reproducibility of the photocurrent produced during the ON/OFF cycles with only a very slight decrease in the photocurrent. This result shows better photostability of the oxyselenide compared to its sulfur-based analogue.

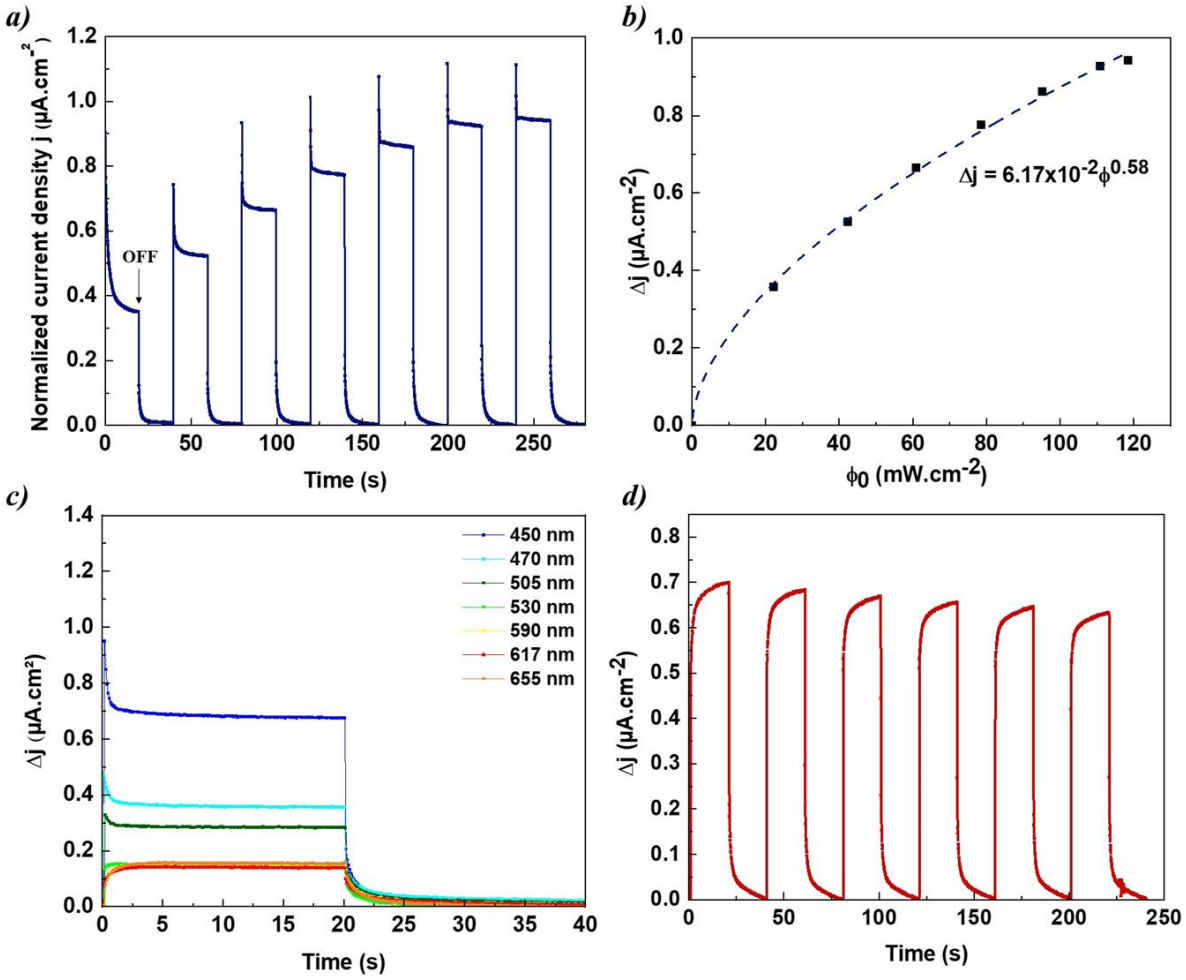

Figure 7 : (a) Transient photocurrent response (V_{bias}=0.4 V under a 450 nm excitation) of $Sr_2Sb_2O_2Se_3$ (b) Evolution of the photocurrent density the power density of light (c) Transient photocurrent response vs. wavelengths (constant light intensity ϕ_0=38 mW cm^{-2}) of $Sr_2Sb_2O_2Se_3$ (d) Transient photocurrent response under solar illumination (100 $mW.cm^{-2}$) for V_{bias}= 0.4 V.

The last electrochemical measurement performed for both compounds was a Mott-Schottky test: the (MS) plot of $1/C^2$ *vs.* applied potential shown in Figure 8a and 8b indicates the conduction type, the concentration of the charge carriers (N) and the flat band potential (E_{fb}).[74] The positive gradient in the Mott-Schottky plot of $1/C^2$ *vs.* V for $Sr_2Sb_2O_2S_3$ is consistent with n-type semiconducting behaviour with a flat band potential E_{fb} of -1.15 V *vs*. Ag/AgCl (reference electrode) or -0.625 V *vs*. RHE (reversible hydrogen electrode).[75] Indeed, a potential measured with respect to Ag/AgCl ($E_{Ag/AgCl}$) can be converted to the RHE scale (E_{RHE}) with expression (4):

$$E_{RHE} = E_{Ag/AgCl} + E^0_{Ag/AgCl} + 0.059.pH \qquad (4)$$

where $E^0_{Ag/AgCl\ vs.SHE}$ is the potential of the Ag/AgCl reference electrode with respect to the standard hydrogen electrode (SHE) fixed at 195 mV. The pH of 0.1 M Na_2SO_4 electrolyte is 5.6.

The Mott-Schottky plot for $Sr_2Sb_2O_2Se_3$ (Figure 8b) is also consistent with n-type semiconducting behavior with a flat band potential E_{fb} of -1.0 V *vs.* Ag/AgCl (reference electrode) or -0.475 V *vs.* RHE (reversible hydrogen electrode).

Depending on the conduction type, the flat band potential serves to locate the valence and conduction band edge positions[75] as it reflects the position of the Fermi level which lies at 0.1 V lower than the conduction band for the n-type semiconductors.[76,77,78] Therefore, this calculated value is close to the calculated CB band edge position (Figure 8c) using the empirical method based on Mulliken electronegativities proposed by Butler and Ginley,[79] and further described by Xu and Schoonen[80] using the following equation:

$$E_{VB,CB} = E_0 + \prod_{M=1}^{n} \chi_M^{j\frac{1}{n}} \pm \frac{E_{gap}}{2} \qquad (5)$$

where $E_{VB,CB}$ corresponds to the positions of the valence and conduction band edges; E_0 to the difference between (NHE) and the vacuum (E_0 = -4.5 eV); χ_M is the electronegativity of the atom *M* in the Mulliken scale with *n* the number of atoms and *j* the stochiometric ratio. Such calculations for the band edge positions were reported in a study by Castelli *et al.*[81] which compares a number of photocatalysts. Our calculations using this method confirm that the band edges for $Sr_2Sb_2O_2S_3$ and $Sr_2Sb_2O_2Se_3$ are appropriate for the redox potential of water and are consistent with the edge positions determined experimentally from Mott-Schottky measurements and the optical band gaps.

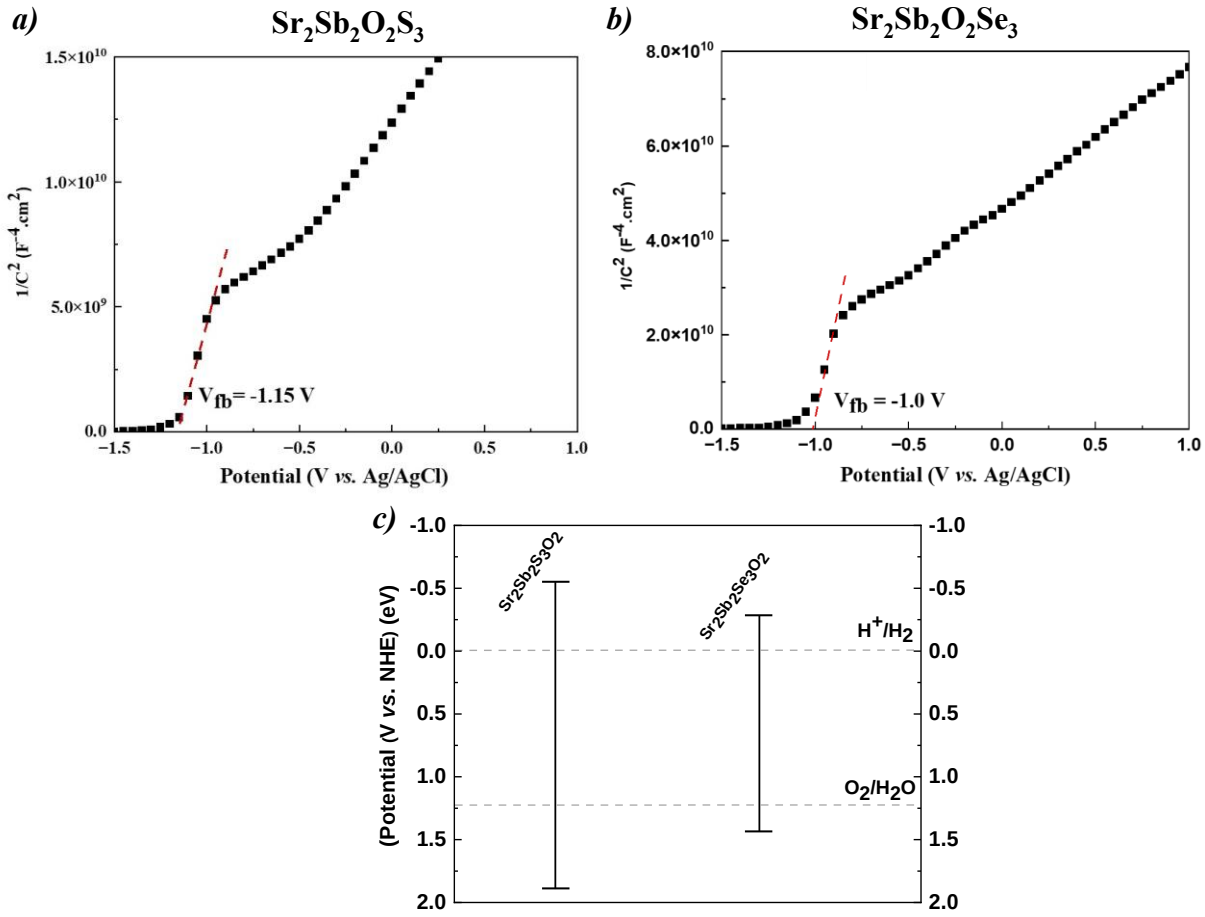

Figure 8 : (a) Mott-Schottky plot for $Sr_2Sb_2O_2S_3$ deposited on ITO/Glass performed at 100 Hz. (b) Mott-Schottky plot for $Sr_2Sb_2O_2Se_3$ deposited on ITO/Glass performed at 1 kHz. (c) Calculated band edges positions for $Sr_2Sb_2O_2S_3$ and $Sr_2Sb_2O_2Se_3$; The levels of H_2 and O_2 evolution are indicated by dashed lines.

Photocatalytic activity. UV-vis spectroscopy was used to follow the kinetics of the photodegradation of Rhodamine B, based on the maximum absorption, allowing the photocatalytic efficiency of $Sr_2Sb_2O_2Q_3$ (Q = S, Se) phases to be quantified. The photocatalytic kinetics at the solid-liquid interface were described using the Langmuir-Hinshelwood model (LH),[82] taking an order 1 for the photodegradation reaction and plotting $Ln(C_0/C)$ *vs.* time to determine the apparent rate constant (k_{app}). Figure 9 shows the corresponding kinetic plots for $Sr_2Sb_2O_2Q_3$ (Q = S, Se) photocatalysts under UV and solar irradiations. Under UV light, both photocatalysts exhibited similar efficiency, where a linear evolution occurred with an apparent rate constant of 2.28×10^{-2} min^{-1} and 1.79×10^{-2} min^{-1} for $Sr_2Sb_2O_2Se_3$ and $Sr_2Sb_2O_2S_3$ respectively. These results

reveal good kinetic performances for both phases and are comparable with other photocatalysts (typically 10^{-2} min^{-1}), such as $La_2Ti_2O_7$ oxide[74] and $Sr_6Cd_2Sb_6S_{10}O_7$ oxysulfide.[20] The performance of both materials decreased under solar irradiation but its striking that quite significant activity was still observed for $Sr_2Sb_2O_2Se_3$ (with rate constant 6.45×10^{-3} min^{-1}). It should be noted that it is difficult to disperse the $Sr_2Sb_2O_2S_3$ phase in solution, and 20 minutes sonication was needed to break up agglomerates and give the best photocatalytic efficiency. $Sr_2Sb_2O_2Se_3$ showed better dispersion (less sonication was needed), and the maximum efficiency is reached more quickly. The kinetics of the photodegradation reaction is usually influenced by the microstructure and the morphology of the photocatalyst as well as its stability in the chosen electrolyte; nonetheless structural parameters (such as polarity, lone pairs) can also influence the outcome of the reaction. The photocatalytic efficiency of $Sr_2Sb_2O_2Q_3$ under solar light ($k = 4.78\times10^{-4}$ and 6.45×10^{-3} min^{-1} for S and Se, respectively) is comparable with copper oxysulfide BiCuSO ($k = 9.1\times10^{-3}$ min^{-1}), capable of degradating an organic pollutant (Congo Red) in aqueous solution under visible light.[83]

Unfortunately, based on the previous photoelectrochemical studies, significant photocorrosion was observed for $Sr_2Sb_2O_2S_3$ upon applying a bias voltage (Figures 6d and supporting information). XRPD patterns of the powder before and after the catalysis and the electrochemical and unit cell parameters measurements (supporting information) don't show any major differences but slight peak broadening might indicate sample degradation, lower crystallinity of the samples after catalysis.

SEM analysis was also carried out on the after-test samples to investigate the grain size and shape (supporting information) and indicated that crystallite size remains comparable. Therefore, photocorrosion cannot be attributed to a structural change but rather to a progressive deterioration (dissolution) of the photoelectrode in the electrolyte. Future work to optimise the electrolyte and film stability would be worthwhile.

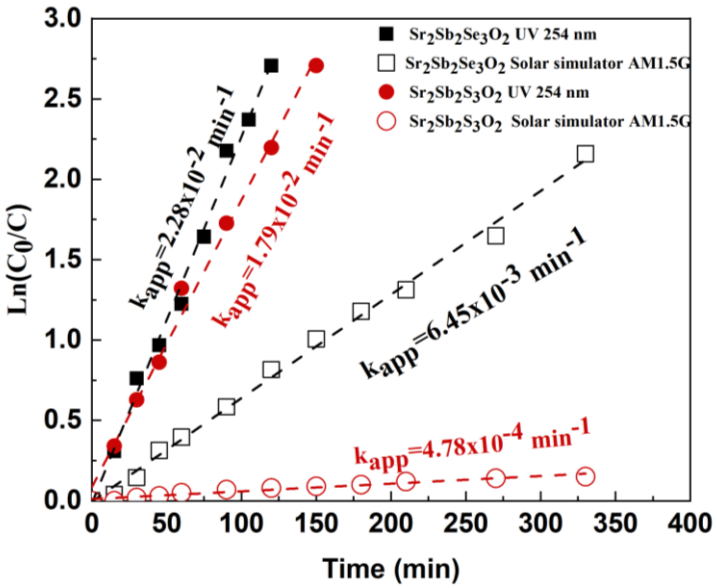

Figure 9 : Langmuir-Hinshelwood kinetic plot for the degradation of Rhodamine B on $Sr_2Sb_2O_2Q_3$ (*Q* = S, Se) under UV (254 nm, 40 W) and Solar (100 $mW.cm^{-2}$) irradiation.

DISCUSSION

The new oxysulfide $Sr_2O_2Sb_2S_3$ described here adopts a crystal structure very similar to its oxyselenide analogue $Sr_2O_2Sb_2Se_3$ reported by Panella et al.[35] A key structural feature in several Sb^{3+} oxychalcogenides the one-dimensional (1D) chains of edge-linked $SbOS_4$ square-based pyramids. In the $Sr_2O_2Sb_2Q_3$ phases discussed here, these form double-chains of $^1_\infty[Sb_2O_2S_{2.5}]^{-3}$ which extend along the [010] direction. In the more complex $Sr_6Cd_2Sb_6Q_{10}O_7$ (*Q* = S, Se) materials,[20,19] single chains of $SbOS_4$ units are edge-linked with SbS_5 chains to form double-chains of $^1_\infty[Sb_2OS_{3.5}]^{-3}$ corner linked to $^1_\infty[CdS_3]^{4-}$ chains, and with isolated $^1_\infty[SbO_{2.5}]^{2-}$ chains also in the structure. These structural features have a direct impact on electron and hole mobilities and therefore on the photocurrent response and photocatalytic activity.

These three antimony oxychalcogenides have low m_e* (0.163, 0.191 and 0.215 for $Sr_2O_2Sb_2Se_3$, $Sr_2O_2Sb_2S_3$ and $Sr_6Cd_2Sb_6S_{10}O_7$,[20] respectively) hence their high mobilities within Sb – S planes, undoubtedly influenced by the effective overlap of Sb 5*p* and S 3*p*/Se 4*p* orbitals which make up the bottom of the conduction band. The Sb – *Q* – Sb angles are constrained by symmetry to be 180° in $Sr_2O_2Sb_2Q_3$ whilst the double-chains in $Sr_6Cd_2Sb_6S_{10}O_7$ are curved, giving Sb – S – Sb angles

of ~168°, (Figure 10) decreasing orbital overlap and bandwidth. In $Sr_2O_2Sb_2Q_3$, the $SbOQ_4$ units within the double-chains are arranged in an anti-fashion and the increased stereochemical activity of the Sb^{3+} $5s^2$ pair for the oxysulfide (Table 2) gives a slightly greater distortion of the $SbOS_4$ square-based pyramids (giving basal-plane S – Sb – S angles ~171°, compared with ~174° Se – Sb – Se angles).

The striking difference between these oxychalcogenides is in their hole effective masses, with extremely low m_h* for $Sr_2O_2Sb_2Se_3$ (Table 1). Theory studies on Sn^{2+} oxides highlight the impact of the extent and direction of orbital overlap between Sn^{2+} 5*s* and O 2*p* orbitals on the curvature of the conduction band and hence the hole mobility.[84] Ha *et al* highlight the importance of Sn – O – Sn angles close to 180° to optimize this hybridization[84] and the greater deviation from 180° for Sb – S – Sb angles in $Sr_6Cd_2Sb_6S_{10}O_7$ (168°) will be detrimental for this mixing. The VBM in $Sr_2O_2Sb_2Q_3$ and in $Sr_6Cd_2Sb_6S_{10}O_7$ are composed of the Sb 5*s* and S/Se *np* states, with the relative energies of these orbitals also determining the degree of stereochemical activity of the Sb $5s^2$ electron pair. Overlap between SbS_5 and $SbOS_4$ lone pairs in $Sr_6Cd_2Sb_6S_{10}O_7$ is hampered by their huge separation in the crystal structure along the direction of the stereochemically-active pairs (see Figure 10), giving rise to a very high hole effective mass (m_h* = 6.5 m_0). By contrast, the Sb $5s^2$ pairs in $Sr_2O_2Sb_2Q_3$ are separated by only ~4 Å along the direction close to the orientation of both electron pairs ($\Gamma \rightarrow$ B). This leads to the exceptionally low m_h* values for $Sr_2O_2Sb_2Se_3$, making it particularly attractive for efficient photoconduction and photocatalysis applications. It would be interesting to carry out conductivity measurements as a function of temperature to allow comparison with other high-mobility materials (e.g. the *p*-type oxysulfide $Cu_2S_2Sr_3Sc_2O_5$.)[85]

The reduced optical band gap of the oxyselenide compared with the oxysulfide (from diffuse reflectance measurements, Figure 3) is consistent with our electronic structure calculations (Figure 4) which revealed a more dispersed conduction band (composed largely of Se 4*p* states) compared with the oxysulfide analogue.

On heating in Ar(g), $Sr_2O_2Sb_2S_3$ decomposes releasing SO (as determined by mass spectrometry). XRPD of the decomposition products (or *in-situ* studies) are needed to confirm the nature of this decomposition, but the reducing atmosphere could favour reduction to metallic antimony and formation of oxides and sulfides of strontium (e.g. $Sr_2O_2Sb_2S_3 \rightarrow SrO(s) + SrS_2(s) + 3Sb(s) + SO(g)$).

In terms of photocurrent response and photocatalytic activity, the results reported here for $Sr_2Sb_2O_2Q_3$ (Q = S, Se) oxychalcogenides reveal their capacity to exhibit photoelectric activity. Their potential to generate a reproducible photocurrent with no applied potential under solar irradiation is striking and makes them promising candidates for photocatalysis in the visible range. This behavior might result from the presence of polar coordination environments within the structure (dipoles across $[SbOSe4]^{7-}$ and $[SbOS4]^{7-}$ units are 15 D and 15.5 D, respectively)[55,19], which makes it possible for the charge carriers to separate without applying an external electric field. In fact, it has been previously reported that introducing polar units, with a built-in electric field, can enhance the electron-hole separation in the photocatalytic material[86,87,88] by facilitating the transfer of the photo-generated pairs to different active sites,[89] resulting in a better photoactivity.[90] Recently, similar results were observed for $Sr_6Cd_2Sb_6O_7Q_{10}$ (Q = S, Se) polar oxysulfide[19,20] and $Na_3VO_2B_6O_{11}$ polar oxide.[91]

The different peak shapes observed in the photocurrent measurements for $Sr_2Sb_2O_2S_3$ and $Sr_2Sb_2O_2Se_3$ (Figure 6a, 7a) indicate that the charge carriers separate faster upon illumination in the case of the oxyselenide (with spikey peaks), while slower separation occurs in the case of the oxysulfide. This is related to the lower effective masses for the oxyselenide, reflecting its more covalent nature. Lower effective masses will allow faster mobility therefore making more probable that the charge carriers reach the surface before recombination.

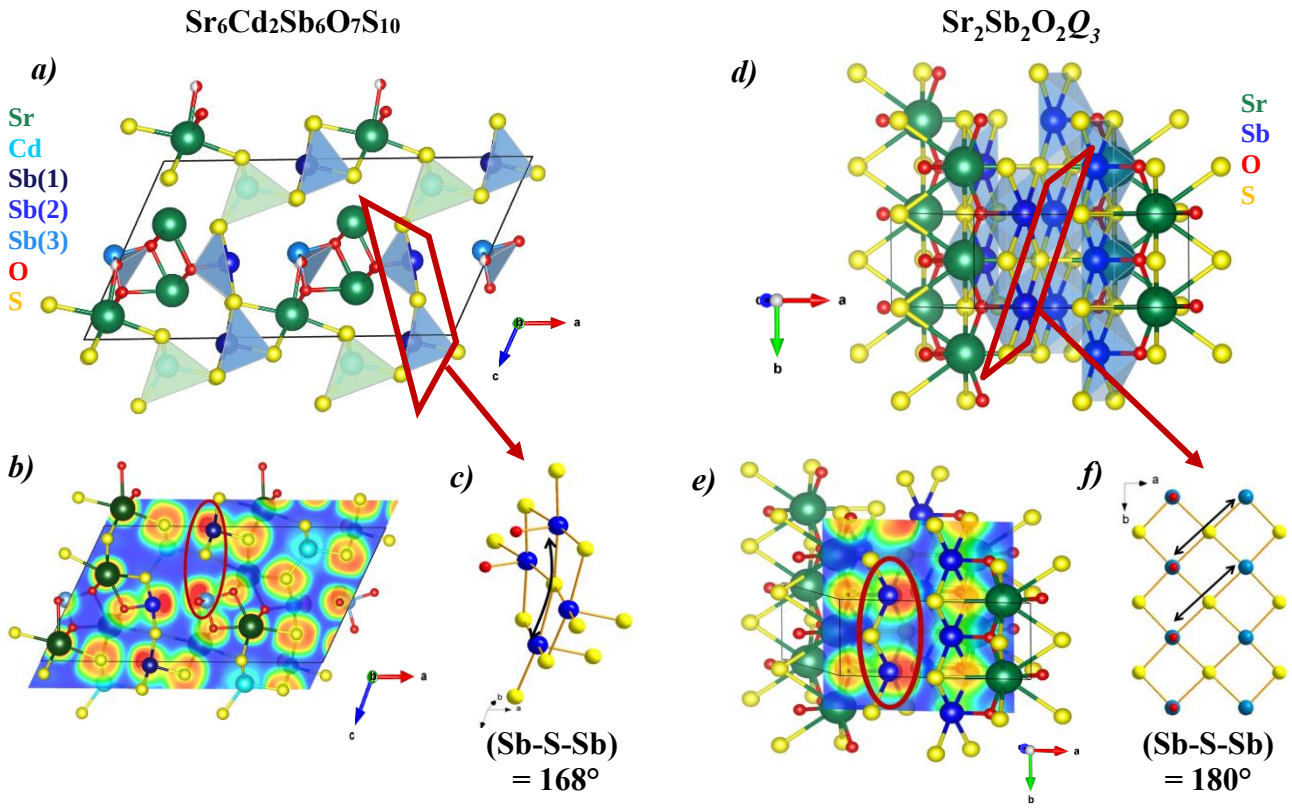

Figure 10 : (a-d) Representation of the structure of $Sr_6Cd_2Sb_6O_7S_{10}$ and $Sr_2Sb_2O_2Q_3$ phases. (b-e) Orbital overlap due to the distance between Sb 5s pairs in $Sr_6Cd_2Sb_6O_7S_{10}$ and $Sr_2Sb_2O_2S_3$, respectively. (c-f) View showing a curvature due to deviation of the Sb-S-Sb angle from 168° in $Sr_6Cd_2Sb_6O_7S_{10}$ to 180° in $Sr_2Sb_2O_2Q_3$.

CONCLUSION

The potential of $Sr_2Sb_2O_2Q_3$ (Q = S, Se) oxychalcogenides for photocatalytic activity is highlighted in this work. These materials may be promising candidates as photocatalysts for water-splitting, under UV and solar irradiation. Several aspects contributed to this activity, including the presence of a stereochemically active lone pair (Sb $5s^2$) and a mixed-anion environment (O:S/Se). The nature of the chalcogenide can tune both the magnitude of the band gap (Figure 3) as well as the effective masses for both the electrons and holes. The exceptionally low hole effective mass for $Sr_2Sb_2O_2Se_3$ can be attributed to the presence of the highly covalent selenide ion (Sb 5*s* - Se 4*p* hybridization). Both $Sr_2Sb_2O_2Q_3$ (Q = S, Se) materials gave photocurrent responses under solar irradiation with no external bias voltage applied, highlighting the importance of intrinsic polarization within the structure. More efficient electron-hole separation and migration was

observed for $Sr_2Sb_2O_2Se_3$ explained by the lower effective masses calculated for this oxyselenide (attributed to its more covalent nature). These two antimony oxychalcogenides showed photocatalytic activity, degrading rhodamine B under solar light. This study illustrates the importance of Sb^{3+} oxychalcogenides for photocatalytic and photocurrent applications as a result of their tunable band gap, stereochemically active $5s^2$ electron pair and resulting high electron and hole mobilities.

ASSOCIATED CONTENT

Supporting Information. The supporting Information is available free of charge.

Rietveld refinement details of $Sr_2Sb_2O_2Q_3$ using room temperature XRPD data; electron microscopy analysis details on $Sr_2Sb_2O_2Q_3$; electronic structure and density of states in the *C*2/*m* model and additional plots of the fat bands and stereochemical activity in $P2_1/c$ model; photocurrent and photocatalysis additional measurements (PDF). Optimized structures parameters and atomic positions for $Sr_2Sb_2O_2Q_3$ in both $P2_1/c$ and *C*2/*m* space groups.

ACKNOWLEDGMENTS

I-Site (ULNE), University of Lille and University of Kent are thanked for cotutelle funding (S. Al Bacha). Durham University is thanked for hosting research visit. Dr. Donna Arnold is thanked for helpful discussions. This study was supported by the French government through the Programme Investissement d'Avenir (I-SITE ULNE / ANR-16-IDEX-0004 ULNE) managed by the Agence Nationale de la Recherche (Project ANION-COMBO). X-Rays Diffractometers are funded by Région NPDC, FEDER, CNRS and MESR. The regional computational cluster supported by Lille University, CPER Nord-Pas-de-Calais/CRDER, France Grille CNRS and FEDER is thanked for providing computational resources. The Chevreul Institute is thanked for its help in the development of this work through the ARCHI-CM project supported by the "Ministère de l'Enseignement Supérieur de la Recherche et de l'Innovation", the region "Hauts-de-France", the ERDF program of the European Union and the "Métropole Européenne de Lille".

REFERENCES

(1) Wachsman, E. D.; Lee, K. T. Lowering the Temperature of Solid Oxide Fuel Cells. *Science* **2011**, *334* (6058), 935–939. https://doi.org/10.1126/science.1204090.

(2) Kong, D.; Zheng, Y.; Kobielusz, M.; Wang, Y.; Bai, Z.; Macyk, W.; Wang, X.; Tang, J. Recent Advances in Visible Light-Driven Water Oxidation and Reduction in Suspension Systems. *Materials Today* **2018**, *21* (8), 897–924.

(3) Ikeda, S.; Hara, M.; Kondo, J. N.; Domen, K.; Takahashi, H.; Okub, T.; Kakihana, M. Preparation of a High Active Photocatalyst, K2La2Ti3O10, by Polymerized Complex Method and Its Photocatalytic Activity of Water Splitting. *Journal of materials research* **1998**, *13* (4), 852–855.

(4) Belver, C.; Adán, C.; Fernández-García, M. Photocatalytic Behaviour of Bi2MO6 Polymetalates for Rhodamine B Degradation. *Catalysis Today* **2009**, *143* (3), 274–281. https://doi.org/10.1016/j.cattod.2008.09.011.
(5) Hashimoto, K.; Irie, H.; Fujishima, A. TiO2 Photocatalysis: A Historical Overview and Future Prospects. *Japanese journal of applied physics* **2005**, *44* (12R), 8269.
(6) Maruska, H. P.; Ghosh, A. K. Photocatalytic Decomposition of Water at Semiconductor Electrodes. *Solar Energy* **1978**, *20* (6), 443–458.
(7) Van Benthem, K.; Elsässer, C.; French, R. Bulk Electronic Structure of SrTiO 3: Experiment and Theory. *Journal of applied physics* **2001**, *90* (12), 6156–6164.
(8) Ji, S. M.; Choi, S. H.; Jang, J. S.; Kim, E. S.; Lee, J. S. Band Gap Tailored Zn (Nb1− x V x) 2O6 Solid Solutions as Visible Light Photocatalysts. *The Journal of Physical Chemistry C* **2009**, *113* (41), 17824–17830.
(9) Subramanian, Y.; Dhanasekaran, A.; Omeiza, L. A.; Somalu, M. R.; Azad, A. K. A Review on Heteroanionic-Based Materials for Photocatalysis Applications. *Catalysts* **2023**, *13* (1), 173.
(10) Yadav, G.; Ahmaruzzaman, M. Multi Anion-Based Materials: Synthesis and Catalytic Applications. *Materials Research Bulletin* **2022**, *152*, 111836.
(11) Katori, H. A.; Adachi, T.; Ohta, H.; Nakamura, S.; Fuwa, A. Magnetism in Two-Leg Ladder Compound Ba6Fe8S15 with Mixed Oxidation State of Iron. *Physics Procedia* **2015**, *75*, 552–556.
(12) Almoussawi, B.; Tomohiri, H.; Kageyama, H.; Kabbour, H. High Pressure Synthesis of the Spin Chain Sulfide Ba9V3S11(S2)2. *European Journal of Inorganic Chemistry* **2021**, *n/a* (n/a). https://doi.org/10.1002/ejic.202001166.
(13) Jia, Y.; Yang, J.; Zhao, D.; Han, H.; Li, C. A Novel Sr2CuInO3S P-Type Semiconductor Photocatalyst for Hydrogen Production under Visible Light Irradiation. *Journal of energy chemistry* **2014**, *23* (4), 420–426.
(14) Hyett, G.; Limburn, G. J.; Iborra Torres, A.; Scanlon, D. O.; Williamson, B.; Stephens, M. Photocatalytic, Structural and Optical Properties of Mixed Anion Solid Solutions Ba3Sc2-XInxO5Cu2S2 and Ba3In2O5Cu2S2-YSey. *Journal of Materials Chemistry A* **2020**, *8*, 19887-19897.
(15) Vonrüti, N. Ferroelectricity and Metastability in (Mixed-Anion) Perovskite Oxides for Improved Solar Water Splitting, 2019.
(16) Clarke, S. J.; Adamson, P.; Herkelrath, S. J.; Rutt, O. J.; Parker, D. R.; Pitcher, M. J.; Smura, C. F. Structures, Physical Properties, and Chemistry of Layered Oxychalcogenides and Oxypnictides. *Inorganic chemistry* **2008**, *47* (19), 8473–8486.
(17) Ueda, K.; Hiramatsu, H.; Hirano, M.; Kamiya, T.; Hosono, H. Wide-Gap Layered Oxychalcogenide Semiconductors: Materials, Electronic Structures and Optoelectronic Properties. *Thin Solid Films* **2006**, *496* (1), 8–15.
(18) Vonrüti, N.; Aschauer, U. Band-Gap Engineering in AB (O x S 1− x) 3 Perovskite Oxysulfides: A Route to Strongly Polar Materials for Photocatalytic Water Splitting. *Journal of Materials Chemistry A* **2019**, *7* (26), 15741–15748.
(19) Wang, R.; Wang, F.; Zhang, X.; Feng, X.; Zhao, C.; Bu, K.; Zhang, Z.; Zhai, T.; Huang, F. Improved Polarization in the Sr6Cd2Sb6O7Se10 Oxyselenide through Design of Lateral Sublattices for Efficient Photoelectric Conversion. *Angewandte Chemie* **2022**, *61*, No. e202206816. https://doi.org/10.1002/anie.202206816
(20) Al Bacha, S.; Saitzek, S.; McCabe, E. E.; Kabbour, H. Photocatalytic and Photocurrent Responses to Visible Light of the Lone-Pair-Based Oxysulfide Sr6Cd2Sb6S10O7. *Inorganic Chemistry* **2022**, *61* (46), 18611–18621.
(21) Wang, Q.; Nakabayashi, M.; Hisatomi, T.; Sun, S.; Akiyama, S.; Wang, Z.; Pan, Z.; Xiao, X.; Watanabe, T.; Yamada, T. Oxysulfide Photocatalyst for Visible-Light-Driven Overall Water Splitting. *Nature materials* **2019**, *18* (8), 827–832.

(22) Miura, A.; Oshima, T.; Maeda, K.; Mizuguchi, Y.; Moriyoshi, C.; Kuroiwa, Y.; Meng, Y.; Wen, X.-D.; Nagao, M.; Higuchi, M. Synthesis, Structure and Photocatalytic Activity of Layered LaOInS 2. *Journal of Materials Chemistry A* **2017**, *5* (27), 14270–14277.
(23) Kabbour, H.; Sayede, A.; Saitzek, S.; Lefevre, G.; Cario, L.; Trentesaux, M.; Roussel, P. Structure of the Water-Splitting Photocatalyst Oxysulfide α-LaOInS 2 and Ab Initio Prediction of New Polymorphs. *Chemical Communications* **2020**, *56* (11), 1645–1648.
(24) Medvedeva, J. E. Magnetically Mediated Transparent Conductors: In 2 O 3 Doped with Mo. *Physical review letters* **2006**, *97* (8), 086401.
(25) Van Hest, M.; Dabney, M. S.; Perkins, J. D.; Ginley, D. S.; Taylor, M. P. Titanium-Doped Indium Oxide: A High-Mobility Transparent Conductor. *Applied Physics Letters* **2005**, *87* (3), 032111.
(26) Hautier, G.; Miglio, A.; Ceder, G.; Rignanese, G.-M.; Gonze, X. Identification and Design Principles of Low Hole Effective Mass P-Type Transparent Conducting Oxides. *Nature communications* **2013**, *4* (1), 1–7.
(27) Medvedeva, J. E.; Hettiarachchi, C. L. Tuning the Properties of Complex Transparent Conducting Oxides: Role of Crystal Symmetry, Chemical Composition, and Carrier Generation. *Physical Review B* **2010**, *81* (12), 125116.
(28) Minami, T. Transparent and Conductive Multicomponent Oxide Films Prepared by Magnetron Sputtering. *Journal of Vacuum Science & Technology A: Vacuum, Surfaces, and Films* **1999**, *17* (4), 1765–1772.
(29) Kamiya, T.; Hosono, H. Material Characteristics and Applications of Transparent Amorphous Oxide Semiconductors. *NPG Asia Materials* **2010**, *2* (1), 15–22.
(30) Fortunato, E.; Barquinha, P.; Martins, R. Oxide Semiconductor Thin-film Transistors: A Review of Recent Advances. *Advanced materials* **2012**, *24* (22), 2945–2986.
(31) Kawazoe, H.; Yanagi, H.; Ueda, K.; Hosono, H. Transparent P-Type Conducting Oxides: Design and Fabrication of Pn Heterojunctions. *Mrs Bulletin* **2000**, *25* (8), 28–36.
(32) Kawazoe, H.; Yasukawa, M.; Hyodo, H.; Kurita, M.; Yanagi, H.; Hosono, H. P-Type Electrical Conduction in Transparent Thin Films of CuAlO2. *Nature* **1997**, *389* (6654), 939–942.
(33) Kim, T.; Yoo, B.; Youn, Y.; Lee, M.; Song, A.; Chung, K.-B.; Han, S.; Jeong, J. K. Material Design of New P-Type Tin Oxyselenide Semiconductor through Valence Band Engineering and Its Device Application. *ACS applied materials & interfaces* **2019**, *11* (43), 40214–40221.
(34) Arai, T.; Iimura, S.; Kim, J.; Toda, Y.; Ueda, S.; Hosono, H. Chemical Design and Example of Transparent Bipolar Semiconductors. *Journal of the American Chemical Society* **2017**, *139* (47), 17175–17180.
(35) Panella, J. R.; Chamorro, J.; McQueen, T. M. Synthesis and Structure of Three New Oxychalcogenides: A2O2Bi2Se3 (A= Sr, Ba) and Sr2O2Sb2Se3. *Chemistry of Materials* **2016**, *28* (3), 890–895.
(36) Coelho, A. TOPAS Academic: General Profile and Structure Analysis Software Fo r Powder Diffraction Datafile, 5th Editio. *Karlsruhe, Germany* **2012**.
(37) Coelho, A. A. TOPAS and TOPAS-Academic: An Optimization Program Integrating Computer Algebra and Crystallographic Objects Written in C++. *Journal of Applied Crystallography* **2018**, *51* (1), 210–218.
(38) Dollase, W. A. Correction of Intensities for Preferred Orientation in Powder Diffractometry: Application of the March Model. *Journal of Applied Crystallography* **1986**, *19* (4), 267–272.
(39) Kresse, G.; Joubert, D. From Ultrasoft Pseudopotentials to the Projector Augmented-Wave Method. *Physical review b* **1999**, *59* (3), 1758.
(40) Blöchl, P. E. Projector Augmented-Wave Method. *Physical review B* **1994**, *50* (24), 17953.

(41) Sun, G.; Kürti, J.; Rajczy, P.; Kertesz, M.; Hafner, J.; Kresse, G. Performance of the Vienna Ab Initio Simulation Package (VASP) in Chemical Applications. *Journal of Molecular Structure: THEOCHEM* **2003**, *624* (1–3), 37–45.
(42) Perdew, J. P.; Burke, K.; Ernzerhof, M. Generalized Gradient Approximation Made Simple. *Physical review letters* **1996**, *77* (18), 3865.
(43) Momma, K. *Visualization for Electronic and Structural Analysis*; 2019.
(44) Maintz, S.; Deringer, V. L.; Tchougréeff, A. L.; Dronskowski, R. LOBSTER: A Tool to Extract Chemical Bonding from Plane-wave Based DFT. *J. Comput. Chem.* **2016**, *37*, 1030.
(45) Dronskowski, R.; Bloechl, P. E. Crystal Orbital Hamilton Populations (COHP): Energy-Resolved Visualization of Chemical Bonding in Solids Based on Density-Functional Calculations. *The Journal of Physical Chemistry* **1993**, *97* (33), 8617–8624.
(46) Deringer, V. L.; Tchougréeff, A. L.; Dronskowski, R. Crystal Orbital Hamilton Population (COHP) Analysis as Projected from Plane-Wave Basis Sets. *The journal of physical chemistry A* **2011**, *115* (21), 5461–5466.
(47) Mentré, O.; Juárez-Rosete, M. A.; Saitzek, S.; Aguilar-Maldonado, C.; Colmont, M.; Arévalo-López, Á. M. S= 1/2 Chain in BiVO3F: Spin Dimers versus Photoanodic Properties. *Journal of the American Chemical Society* **2021**, *143* (18), 6942–6951.
(48) Kubelka, P.; Munk, F. A Contribution to the Optics of Pigments. *Z. Tech. Phys* **1931**, *12* (593), 193.
(49) Tauc, J.; Grigorovici, R.; Vancu, A. Optical Properties and Electronic Structure of Amorphous Germanium. *physica status solidi (b)* **1966**, *15* (2), 627–637.
(50) Jiang, S.; Liu, Y.; Xu, J. Rare Earth Oxynitrides: Promising Visible-Light-Driven Photocatalysts for Water Splitting. *Materials Advances* **2021**, *2* (4), 1190–1203.
(51) Siritanaratkul, B.; Maeda, K.; Hisatomi, T.; Domen, K. Synthesis and Photocatalytic Activity of Perovskite Niobium Oxynitrides with Wide Visible-light Absorption Bands. *ChemSusChem* **2011**, *4* (1), 74–78.
(52) Lei, S.; Cheng, D.; Gao, X.; Fei, L.; Lu, W.; Zhou, J.; Xiao, Y.; Cheng, B.; Wang, Y.; Huang, H. A New Low-Temperature Solution Route to Aurivillius-Type Layered Oxyfluoride Perovskites Bi2MO5F (M= Nb, Ta) as Photocatalysts. *Applied Catalysis B: Environmental* **2017**, *205*, 112–120.
(53) Ishikawa, A.; Takata, T.; Kondo, J. N.; Hara, M.; Kobayashi, H.; Domen, K. Oxysulfide Sm2Ti2S2O5 as a Stable Photocatalyst for Water Oxidation and Reduction under Visible Light Irradiation (Λ≤ 650 Nm). *Journal of the American Chemical Society* **2002**, *124* (45), 13547–13553.
(54) Ishikawa, A.; Takata, T.; Matsumura, T.; Kondo, J. N.; Hara, M.; Kobayashi, H.; Domen, K. Oxysulfides Ln2Ti2S2O5 as Stable Photocatalysts for Water Oxidation and Reduction under Visible-Light Irradiation. *J. Phys. Chem. B* **2004**, *108* (8), 2637–2642. https://doi.org/10.1021/jp036890x.
(55) Wang, R.; Liang, F.; Wang, F.; Guo, Y.; Zhang, X.; Xiao, Y.; Bu, K.; Lin, Z.; Yao, J.; Zhai, T. Sr6Cd2Sb6O7S10: Strong SHG Response Activated by Highly Polarizable Sb/O/S Groups. *Angewandte Chemie International Edition* **2019**, *58* (24), 8078–8081.
(56) Allen, J. P.; Carey, J. J.; Walsh, A.; Scanlon, D. O.; Watson, G. W. Electronic Structures of Antimony Oxides. *The Journal of Physical Chemistry C* **2013**, *117* (28), 14759–14769.
(57) Wang, X.; Li, Z.; Kavanagh, S. R.; Ganose, A. M.; Walsh, A. Lone Pair Driven Anisotropy in Antimony Chalcogenide Semiconductors. *arXiv preprint arXiv:2109.08117* **2021**.
(58) Wang, V.; Xu, N.; Liu, J.-C.; Tang, G.; Geng, W.-T. VASPKIT: A User-Friendly Interface Facilitating High-Throughput Computing and Analysis Using VASP Code. *Computer Physics Communications* **2021**, *267*, 108033.
(59) Gamon, J.; Giaume, D.; Wallez, G.; Labégorre, J.-B.; Lebedev, O.; Al Rahal Al Orabi, R.; Haller, S.; Le Mercier, T.; Guilmeau, E.; Maignan, A. Substituting Copper with Silver in the BiMOCh Layered Compounds (M= Cu or Ag; Ch= S, Se, or Te): Crystal, Electronic Structure, and Optoelectronic Properties. *Chemistry of Materials* **2018**, *30* (2), 549–558.

(60) Hiramatsu, H.; Ueda, K.; Ohta, H.; Hirano, M.; Kikuchi, M.; Yanagi, H.; Kamiya, T.; Hosono, H. Heavy Hole Doping of Epitaxial Thin Films of a Wide Gap P-Type Semiconductor, LaCuOSe, and Analysis of the Effective Mass. *Applied physics letters* **2007**, *91* (1), 012104.
(61) Wang, X.; Li, Z.; Kavanagh, S. R.; Ganose, A. M.; Walsh, A. Lone Pair Driven Anisotropy in Antimony Chalcogenide Semiconductors. *Physical Chemistry Chemical Physics* **2022**, *24* (12), 7195–7202.
(62) Mohn, C. E.; Stølen, S. Influence of the Stereochemically Active Bismuth Lone Pair Structure on Ferroelectricity and Photocalytic Activity of Aurivillius Phase Bi 2 WO 6. *Physical Review B* **2011**, *83* (1), 014103.
(63) Hu, C.; Zhang, B.; Lei, B.-H.; Pan, S.; Yang, Z. Advantageous Units in Antimony Sulfides: Exploration and Design of Infrared Nonlinear Optical Materials. *ACS applied materials & interfaces* **2018**, *10* (31), 26413–26421.
(64) Hu, C.; Mutailipu, M.; Wang, Y.; Guo, F.; Yang, Z.; Pan, S. The Activity of Lone Pair Contributing to SHG Response in Bismuth Borates: A Combination Investigation from Experiment and DFT Calculation. *Physical Chemistry Chemical Physics* **2017**, *19* (37), 25270–25276.
(65) Walsh, A.; Payne, D. J.; Egdell, R. G.; Watson, G. W. Stereochemistry of Post-Transition Metal Oxides: Revision of the Classical Lone Pair Model. *Chemical Society Reviews* **2011**, *40* (9), 4455–4463.
(66) Payne, D. J.; Egdell, R. G.; Walsh, A.; Watson, G. W.; Guo, J.; Glans, P.-A.; Learmonth, T.; Smith, K. E. Electronic Origins of Structural Distortions in Post-Transition Metal Oxides: Experimental and Theoretical Evidence for a Revision of the Lone Pair Model. *Physical review letters* **2006**, *96* (15), 157403.
(67) Shaikh, S. K.; Inamdar, S. I.; Ganbavle, V. V.; Rajpure, K. Y. Chemical Bath Deposited ZnO Thin Film Based UV Photoconductive Detector. *Journal of Alloys and Compounds* **2016**, *664*, 242–249.
(68) Inamdar, S.; Ganbavle, V.; Shaikh, S.; Rajpure, K. Effect of the Buffer Layer on the Metal–Semiconductor–Metal UV Photodetector Based on Al-doped and Undoped ZnO Thin Films with Different Device Structures. *physica status solidi (a)* **2015**, *212* (8), 1704–1712.
(69) Zhao, Q.; Wang, W.; Carrascoso-Plana, F.; Jie, W.; Wang, T.; Castellanos-Gomez, A.; Frisenda, R. The Role of Traps in the Photocurrent Generation Mechanism in Thin InSe Photodetectors. *Materials Horizons* **2020**, *7* (1), 252–262.
(70) Shi, Y.-F.; Li, X.-F.; Zhang, Y.-X.; Lin, H.; Ma, Z.; Wu, L.-M.; Wu, X.-T.; Zhu, Q.-L. [(Ba19Cl4)(Ga6Si12O42S8)]: A Two-Dimensional Wide-Band-Gap Layered Oxysulfide with Mixed-Anion Chemical Bonding and Photocurrent Response. *Inorganic chemistry* **2019**, *58* (10), 6588–6592.
(71) Ogisu, K.; Ishikawa, A.; Shimodaira, Y.; Takata, T.; Kobayashi, H.; Domen, K. Electronic Band Structures and Photochemical Properties of La− Ga-Based Oxysulfides. *The Journal of Physical Chemistry C* **2008**, *112* (31), 11978–11984.
(72) Parkinson, B.; Turner, J.; Peter, L.; Lewis, N.; Sivula, K.; Domen, K.; Bard, A. J.; Fiechter, S.; Collazo, R.; Hannappel, T. *Photoelectrochemical Water Splitting: Materials, Processes and Architectures*; Royal Society of Chemistry, 2013.
(73) Peter, L. M. Energetics and Kinetics of Light-Driven Oxygen Evolution at Semiconductor Electrodes: The Example of Hematite. *Journal of Solid State Electrochemistry* **2013**, *17*, 315–326.
(74) Leroy, S.; Blach, J.-F.; Huvé, M.; Léger, B.; Kania, N.; Henninot, J.-F.; Ponchel, A.; Saitzek, S. Photocatalytic and Sonophotocatalytic Degradation of Rhodamine B by Nano-Sized La2Ti2O7 Oxides Synthesized with Sol-Gel Method. *Journal of Photochemistry and Photobiology A: Chemistry* **2020**, *401*, 112767. https://doi.org/10.1016/j.jphotochem.2020.112767.
(75) Bott, A. W. Electrochemistry of Semiconductors. *Current Separations* **1998**, *17*, 87–92.
(76) Matsumoto, Y.; Omae, M.; Watanabe, I.; Sato, E. Photoelectrochemical Properties of the Zn-Ti-Fe Spinel Oxides. *Journal of the Electrochemical Society* **1986**, *133* (4), 711.

(77) Kalanur, S. S. Structural, Optical, Band Edge and Enhanced Photoelectrochemical Water Splitting Properties of Tin-Doped WO3. *Catalysts* **2019**, *9* (5), 456.
(78) Lin, L.; Lin, J. M.; Wu, J. H.; Hao, S. C.; Lan, Z. Photovoltage Enhancement of Dye Sensitised Solar Cells by Using ZnO Modified TiO2 Electrode. *null* **2010**, *14* (5), 370–374. https://doi.org/10.1179/143307510X12820854748791.
(79) Butler, M.; Ginley, D. Prediction of Flatband Potentials at Semiconductor-electrolyte Interfaces from Atomic Electronegativities. *Journal of the Electrochemical Society* **1978**, *125* (2), 228.
(80) Xu, Y.; Schoonen, M. A. The Absolute Energy Positions of Conduction and Valence Bands of Selected Semiconducting Minerals. *American Mineralogist* **2000**, *85* (3–4), 543–556.
(81) Castelli, I. E.; Landis, D. D.; Thygesen, K. S.; Dahl, S.; Chorkendorff, I.; Jaramillo, T. F.; Jacobsen, K. W. New Cubic Perovskites for One-and Two-Photon Water Splitting Using the Computational Materials Repository. *Energy & Environmental Science* **2012**, *5* (10), 9034–9043.
(82) Ohtani, B. Photocatalysis by Inorganic Solid Materials: Revisiting Its Definition, Concepts, and Experimental Procedures. *Advances in Inorganic Chemistry* **2011**, *63*, 395–430.
(83) Luo, Y.; Qiao, L.; Wang, H.; Lan, S.; Shen, Y.; Lin, Y.; Nan, C. Bismuth Oxysulfide and Its Polymer Nanocomposites for Efficient Purification. *Materials* **2018**, *11* (3), 447.
(84) Ha, V.-A.; Ricci, F.; Rignanese, G.-M.; Hautier, G. Structural Design Principles for Low Hole Effective Mass S-Orbital-Based p-Type Oxides. *Journal of Materials Chemistry C* **2017**, *5* (23), 5772–5779.
(85) Liu, M.-L.; Wu, L.-B.; Huang, F.-Q.; Chen, L.-D.; Chen, I. A Promising P-Type Transparent Conducting Material: Layered Oxysulfide [Cu2S2][Sr3Sc2O5]. *Journal of Applied Physics* **2007**, *102* (11).
(86) Dong, X.-D.; Zhang, Y.-M.; Zhao, Z.-Y. Role of the Polar Electric Field in Bismuth Oxyhalides for Photocatalytic Water Splitting. *Inorganic Chemistry* **2021**, *60* (12), 8461–8474.
(87) Lou, Z.; Wang, P.; Huang, B.; Dai, Y.; Qin, X.; Zhang, X.; Wang, Z.; Liu, Y. Enhancing Charge Separation in Photocatalysts with Internal Polar Electric Fields. *ChemPhotoChem* **2017**, *1* (5), 136–147.
(88) Dong, X.-D.; Yao, G.-Y.; Liu, Q.-L.; Zhao, Q.-M.; Zhao, Z.-Y. Spontaneous Polarization Effect and Photocatalytic Activity of Layered Compound of BiOIO3. *Inorganic Chemistry* **2019**, *58* (22), 15344–15353.
(89) Chen, F.; Huang, H.; Guo, L.; Zhang, Y.; Ma, T. The Role of Polarization in Photocatalysis. *Angewandte Chemie International Edition* **2019**, *58* (30), 10061–10073.
(90) Guo, Y.; Shi, W.; Zhu, Y. Internal Electric Field Engineering for Steering Photogenerated Charge Separation and Enhancing Photoactivity. *EcoMat* **2019**, *1* (1), e12007.
(91) Chen, J.; Zhai, Y.; Yu, Y.; Luo, J.; Fan, X. Spatial Separation of Photo-Induced Charge Carriers in a Na3VO2B6O11 Polar Material and Its Enhanced Photocatalytic Activity. *Applied Surface Science* **2021**, *556*, 149809.

TOC Graphic

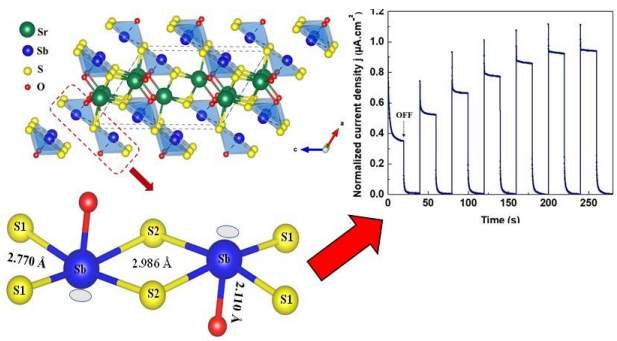
Sr
Sb
S
O
S1
S2
Sb
2.770 Å
2.986 Å
2.110 Å
OFF
Normalized current density | (μA.cm⁻²)
Time (s)